Investigating the cloud radiative effect of Arctic cirrus

Andreas Marsing[1], Ralf Meerkötter[1], Romy Heller[1], Stefan Kaufmann[1], Tina Jurkat-Witschas[1],
Martina Krämer[2,3], Christian Rolf[2], and Christiane Voigt[1,3]

[1]Institute of Atmospheric Physics, German Aerospace Center (DLR), Oberpfaffenhofen, Germany
[2]Institute for Energy and Climate Research (IEK-7), Research Center Jülich, Jülich, Germany
[3]Institute for Atmospheric Physics, Johannes Gutenberg University, Mainz, Germany

Correspondence: Andreas Marsing (andreas.marsing@dlr.de)

Abstract. The radiative energy budget in the Arctic undergoes a rapid transformation compared to global mean changes. Understanding the role of cirrus in this system is vital, as they interact with short- and long-wave radiation and the presence of cirrus can be decisive as to a net gain or loss of radiative energy in the polar atmosphere.

In an effort to derive radiative properties of cirrus in a real scenario in this sensitive region, we use in-situ measurements of ice water content (IWC) performed during the POLSTRACC aircraft campaign in the boreal winter and spring 2015/2016 employing the German research aircraft HALO. A large dataset of IWC measurements of mostly thin cirrus at high northern latitudes was collected in the upper troposphere and also frequently in the lowermost stratosphere. From this dataset we selected vertical profiles that sampled the complete vertical extent of cirrus cloud layers. These profiles exhibit a vertical IWC structure that will be shown to control the instantaneous radiative effect both in the long and short wavelength regimes in the polar winter.

We perform radiative transfer calculations with the UVSPEC model from the libRadtran program package in a one-dimensional column between the surface and the top of the atmosphere (TOA), taking as input the IWC profiles, as well as the state of the atmospheric column at the time of measurement, as given by weather forecast products. In parameter studies, we vary the surface albedo and solar zenith angle in ranges typical for the Arctic region. We find the strongest (positive) radiative forcing of cirrus over bright snow, whereas the forcing is mostly weaker and even ambiguous over the open ocean in winter and spring. The IWC structure over several kilometres in the vertical affects the irradiance at the TOA through the distribution of optical thickness. A strong heating rate profile within the cloud drives dynamical processes and contributes to the thermal stratification at the tropopause.

Our case studies highlight the importance of a detailed resolution of cirrus clouds and consideration of surface albedo for estimations of the radiative energy budget in the Arctic.

1 Introduction

Cirrus clouds are water ice clouds that exist at temperatures below the homogeneous freezing threshold of about 235 K. The required temperatures and humidity conditions are found in the upper troposphere and sometimes lowermost stratosphere, leading to an average global coverage of at least 20 %. Cirrus clouds form in ice super-saturated regions in the presence of

25 suitable nuclei that may be aerosol of different kind, solid or liquid, or by freezing of (supercooled) liquid droplets in ascending air masses (Heymsfield et al., 2017).

The impact of cirrus on the radiative energy budget of the atmosphere can be differentiated by direct and indirect effects. The direct effect is absorption and re-emission of thermal (longwave) radiation and scattering of solar (shortwave) radiation. Indirect or secondary effects arise through the redistribution of water vapour and trough heterogeneous physical (trapping,

30 release, e.g. Kärcher and Voigt, 2006; Kärcher et al., 2009; Voigt et al., 2006) and chemical reactions with radiatively active compounds, such as ozone-depleting substances (e.g. von Hobe et al., 2011; Solomon et al., 1997; Borrmann et al., 1996).

Cirrus occurrence and radiative properties are prone to unavoidable or intentional anthropogenic influence through the introduction of ice nucleating particles and precursors (Hoose and Möhler, 2012), including aircraft emissions (Kärcher, 2018), and through the evolution of atmospheric humidity as a feedback to changing climate as a whole.

35 Cirrus are more abundant and thicker in the tropics and mid-latitudes, but there is also considerable coverage in the high latitude and polar regions. There, the low elevation of the sun and complete absence of sunlight in polar nights reduce the shortwave effect (Hong and Liu, 2015). It is known that the microphysical properties of cirrus, such as particle number concentration, size distribution and shape, depend on the nuclei and the environmental conditions during nucleation, such as updraft speeds (e.g. Kärcher and Jensen, 2017; Joos et al., 2014; Krämer et al., 2020). In addition, the Arctic surface climate currently

40 undergoes a much more rapid warming transition than the rest of the globe, known as Arctic amplification, which also changes the spatial and temporal patterns of the surface albedo as sea ice and continental ice retreat (Wendisch et al., 2017; Shupe et al., 2022). Therefore the question has not yet been answered satisfactorily how Arctic cirrus impact the radiation budget: in which direction, to which extent, and under which circumstances, that will change in the coming decades.

Although cirrus are regularly observed from space with active (e.g. Sassen et al., 2008; Pitts et al., 2018) and passive (e.g.

45 Strandgren et al., 2017) sensors, in situ measurements are needed for the closure of the links between the physical appearance of cirrus ice crystals and their bulk radiative properties (Thornberry et al., 2017; Krisna et al., 2018; Ewald et al., 2021). There have been some in situ studies on Arctic cirrus clouds in the past: the Polar Stratospheric Aerosol Experiment (POLSTAR) missions 1997/1998 (Schiller et al., 1999), the European Polar Stratospheric Cloud and Lee Wave Experiment (EUPLEX) in January-February 2003 and the ENVISAT validation experiments in October 2002/March 2003, with measurements of ice water content

50 (IWC) up to 68° N (summary in Schiller et al., 2008); the Stratospheric Aerosol and Gas Experiment (SAGE) III Ozone Loss and Validation Experiment (SOLVE) in 1999–2000 with measurements of IWC and particle size distribution (Schiller et al., 2002; Hallar et al., 2004). The mentioned missions accumulate to a total of 15 flights and contributed a significant part to our current picture of cirrus in the Arctic. Nevertheless these are few studies compared to much more comprehensive observations in the tropics and at mid latitudes (e.g. Voigt et al., 2007; Thornberry et al., 2017; Heymsfield et al., 2017; Krämer et al.,

55 2016, 2020).

The present work introduces a novel dataset of in situ IWC measurements carried out during the Polar Stratosphere in a Changing Climate (POLSTRACC) campaign employing the German High Altitude and Long Range research aircraft HALO (Oelhaf et al., 2019). The campaign was based in Kiruna, Sweden (67.5° N, 20.3° E) and spanned the boreal winter/spring season from 17 December 2015 to 18 March 2016 with 18 science flights and 156 flight hours. The campaign accommodated

Atmospheric
Chemistry
and Physics
Discussions

60 a number of different science goals, including trace gas composition in the upper troposphere and lower stratosphere (Marsing et al., 2019; Johansson et al., 2019; Braun et al., 2019; Keber et al., 2020; Ziereis et al., 2022), gravity waves (Krisch et al., 2020) and polar stratospheric clouds (Voigt et al., 2018). Therefore, the flight strategy often times needed to avoid extended sections in cirrus clouds. Nevertheless, a total of 7.2 h inside cirrus during 44 individual events were recorded.

The flights included several climb or descent profiles through cirrus clouds, predominantly located just below the thermal
65 tropopause. In this study, we take advantage of these IWC profiles and embed them in the corresponding atmospheric column of temperature and trace gases from European Centre for Medium-Range Weather Forecasts (ECMWF) model analysis. First, this lets us observe the cirrus in relation to the local tropopause and the characteristic of a tropopause inversion layer (TIL) above. Second, it enables radiative transfer calculations that help understand the effect of these (thin) high latitude ice clouds on the atmospheric radiation budget as a whole and on the heating rate profile inside the cloud layer in detail. This constitutes the
70 link between realistic profiles (as they are directly measured) and their impact on local dynamics and radiative energy budget.

An earlier study by Feofilov et al. (2015) uses spaceborne radar, lidar and radiance measurements to derive the radiative impact at the top of the atmosphere (TOA) of differently shaped IWC profiles including global variations. In general we can confirm the effect of an inhomogeneous vertical IWC distribution. Contrastingly, our study focuses on thin high latitude cirrus and we demonstrate the radiative effects, including heating rate, in the whole atmospheric column. This also constitutes a link
75 to cloud dynamics modelling studies that investigate the interaction of heating rate profiles with ice supersaturation, vertical velocity and particle nucleation and growth (Fusina et al., 2007; Fusina and Spichtinger, 2010). Bucholtz et al. (2010) present directly measured heating rates in thin tropical cirrus and highlight the importance of further observations to improve the understanding of the radiative effects of cirrus.

Our findings still rely on various assumptions regarding ice crystal microphysics. Hence they provide a path to further
80 substantiate the results using recent observations from the dedicated HALO mission CIRRUS-HL on cirrus in high latitudes.

The manuscript is laid out as follows: Section 2 contains the experimental acquisition of in situ IWC data. An overview and statistical characteristics of sampled Arctic cirrus clouds are given in Sec. 3, whereas Sec. 4 breaks the observations down to the detailed profiles. Section 5 elaborates on the radiative transfer calculations. Section 6 contains the discussion and summary of the material.

85 ## 2   In situ measurements of IWC

The IWC measurement was performed with the WAter vapoR ANalyzer (WARAN) laser hygrometer. It uses the absorption of the $1.37\,\mu m$ line from a InGaAs tunable diode laser (TDL) in a closed measurement cell in order to derive the concentration of water vapour (Voigt et al., 2014) in the sample flow. The sensor is the commercial WVSS-II by SpectraSensors Inc. with a modified inlet line and connected to a Trace Gas Inlet (TGI) at the fuselage of HALO. The measurement range is 50–
90 $10000\,ppmv$, with a precision of $5\,\%$ or $50\,ppmv$, whichever is greater. Values are sampled at a frequency of 0.3–0.4 Hz.

Whereas the instrument design and data treatment compensate for drifts due to changing environmental conditions, such as temperature and pressure (Heller, 2018), slow degradation requires repeated calibration within months. A calibration for the

POLSTRACC campaign was performed afterwards on 28 July 2016 using a gauged dew point mirror (MBW 373-LX). The result is a linear correction function

$$H_2O_{calibrated} = a + b \cdot H_2O_{WARAN}, \tag{1}$$

where H_2O_{WARAN} denotes the output water vapour mixing ratio from WARAN and $H_2O_{corrected}$ is the calibrated mixing ratio, both in ppmv. The calibration coefficients a and b are determined piecewise:

$$
\begin{aligned}
a &= 3.756\,\text{ppmv}, & b &= 1.045 & \text{for} & \quad H_2O_{WARAN} \leq 70\,\text{ppmv}, \\
a &= 12.619\,\text{ppmv}, & b &= 0.944 & \text{for} & \quad H_2O_{WARAN} > 70\,\text{ppmv}.
\end{aligned} \tag{2}
$$

Through a forward facing trace gas inlet with an inner diameter of $9.55\,\text{mm}$ and stainless steel tubing, WARAN samples the total water content of the atmosphere, composed of gaseous, liquid and solid (ice) fractions. The condensed phases are evaporated along the heated inlet line to feed the instrument only with water vapour. In cirrus clouds that contain only ice, the ice water content (IWC) can be calculated by subtracting the gas phase water content (GWC) from the measurement. Due to a lack of an independent GWC measurement in clouds during the POLSTRACC campaign, the saturation mixing ratio is used as a first order approximation, calculated from the Clausius-Clapeyron equation (Heller, 2018).

Sub-isokinetic sampling due to a lower inlet flow velocity compared the speed of airflow around the fuselage leads to an enhancement of particles in the inlet flow. Therefore, a correcting "enhancement factor" (EF) needs to be applied to the IWC measurement. Following the rationale in Heller (2018), the EF for typical high latitude cirrus, where significant contributions to the IWC are contained in particles with radii larger than $20\,\mu m$ (Wolf et al., 2018), can be calculated as

$$EF = \frac{u_a}{u_0} \tag{3}$$

with the known airspeed u_a and inlet velocity u_0 (Schiller et al., 1999). This approximation is independent of the precise particle size distribution and takes values of about 70 to 80 for the POLSTRACC measurements. Such high EF values effectively lower the detection limit of the corrected IWC to below $1\,\text{ppmv}$. The error in calculating the EF is $\pm 5\,\%$, leading to a precision of $10\,\%$ for IWC measurements.

Another major uncertainty in airborne IWC measurements arises from further enhancement or depletion of particles of different sizes in the flow around the aircraft until the sampling position. Afchine et al. (2018) studied this effect in detail, including data from the HALO mission ML-CIRRUS (Voigt et al., 2017), and found particular ramifications for cabin instruments with inlet positions at the fuselage. Afchine et al. (2018) found that the IWC from WARAN was mostly systematically higher than the IWC from FISH (Meyer et al., 2015), a Lyman-α hygrometer that samples total water in a similar way, but at a different position. This comparison is repeated with the POLSTRACC data in Fig. 1. Here, a systematic deviation is not obvious, as the correlation between both instruments is well centred on the 1:1 line and there are no pronounced off-centred branches. More than $50\,\%$ of the measurements coincide within a factor 2 above $1\,\text{ppmv}$. In a linear regression, the coefficient of determination $R^2 = 0.73$ is smaller compared to Afchine et al. (2018), but the intercept $y_0 = -0.040$ is closer to zero and the slope $m = 0.952$ closer to identity. This enhanced comparability is attributed to improved calibration and a precise
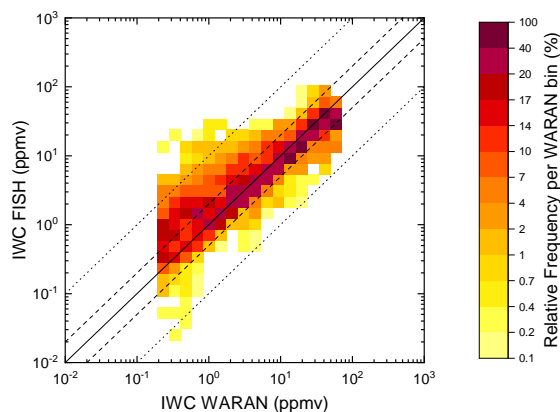
Figure 1. Comparison of ice water content (IWC) from the WARAN and FISH instruments for cirrus measurements during the POLSTRACC campaign. The shading indicates the distribution of data within each WARAN bin. Note the double logarithmic axes and the logarithmic colour scale. The solid line represents the 1:1 identity. The dashed lines denote a deviation of factor 2, and the dotted lines a deviation of factor 10. Accounting for the detection limit, WARAN data are clipped below 0.2 ppmv.

synchronisation of data streams. It also shows that the different positions of both inlets, which are about 3 m apart along the
125 length of the fuselage, have a less pronounced impact on the observable IWC than previously thought. Nevertheless, we need to
clarify that the IWC measurements from both instruments through roof-mounted TGIs are strongly affected by enrichment or
loss of ice particles due to their inertia in the flow around the aircraft's fuselage. Afchine et al. (2018) could quantify this effect
for the HALO aircraft with comparing IWC and particle size distribution measurements at the much less affected wing probe
position, where IWC deviations by up to one order of magnitude were observed at a significant frequency. This flaw cannot be
130 easily overcome for the POLSTRACC data without knowledge about the particle size distribution. In the study of the impact on
radiation of the observed IWC distributions in Sec. 5, we therefore address the effects of underestimated IWC sampling. There,
we test the sensitivity of our results to an underestimated IWC by re-evaluating all calculations with IWC profiles multiplied
by a factor of 5, which corresponds to the average deviation seen for the FISH instrument in the worst particle size regime
above 25 µm (Afchine et al., 2018).

3 Statistics of Arctic cirrus sampling

The POLSTRACC mission accommodated several scientific objectives that made use of the high ceiling altitude, long range and
heavy payload capabilities of the HALO research aircraft (Oelhaf et al., 2019). For the observation of trace gas composition
and gravity waves, the flight strategy often needed to avoid extended in-cloud sections. Therefore the data set represents a
relatively random sampling of cirrus at the middle to high latitudes. Nevertheless, the 18 science flights spanning 156 flight
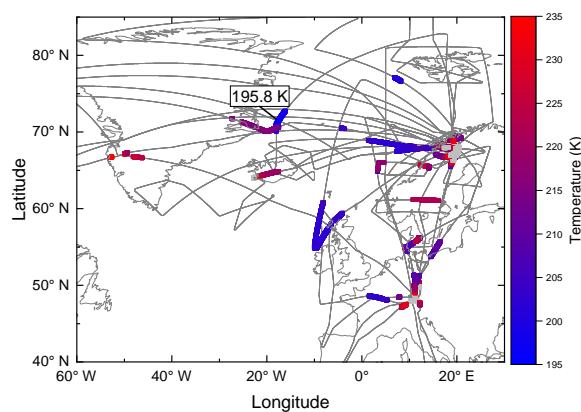
Figure 2. Map of the North Atlantic showing the flight tracks of the POLSTRACC campaign. Coloured sections denote IWC measurements from the WARAN instrument. The colour coding indicates the temperature during these sections, where red is warmer than blue, and grey colors are above 235 K.

140   hours yielded an accumulated residence time of 7.2 h inside cirrus clouds during 44 individual events, as calculated from the number of WARAN IWC measurements at temperatures below 235 K.

Figure 2 shows the IWC measurements as coloured sections of the POLSTRACC flight tracks. It can be seen that there are many shorter sections around the landing sites during the campaign: Oberpfaffenhofen, Germany (EDMO); Kiruna, Sweden (ESNQ); Kangerlussuaq, Greenland (BGSF). Cloud layers there were often crossed during approaches and departures. Some
145   more extended sections in mid-flight are found intermittently. The colour coding shows the range of temperatures during these cirrus encounters. The minimum temperature recording during an IWC event was 195.8 K.

For the IWC as an accessible bulk property, previous studies set up climatologies that relate the IWC to temperature (Schiller et al., 2008; Krämer et al., 2016) and other properties such as effective radius and number concentration (e.g. Krämer et al., 2020; Luebke et al., 2013; Liou et al., 2008), and broke them down to different latitudes on Earth and different cloud formation
150   pathways. Schiller et al. (2008) and later Luebke et al. (2013) collected the range of airborne cirrus measurements from different campaigns as a function of latitude and temperature. In Fig. 3 the POLSTRACC measurements are added to this scheme found in Luebke et al. (2013). The broad latitudinal range of the POLSTRACC measurements can be seen. While many domains have been covered by previous missions, the figure shows that the new data also extend into gaps that were not filled before. This concerns in particular the lower temperatures below 210 K down to 198 K at the mid latitudes between 45 to 60° N. A
155   4 h fraction of the campaign data was sampled north of 60° N and a significant extension to existing data could be made at 65° N over the whole temperature range. Measurements north of 70° N are generally sparse, and POLSTRACC can extend the coverage slightly for the cold cirrus below 200 K. Still there is much room left open temperaturewise, but also in the latitudinal coverage between 70° N and the pole.
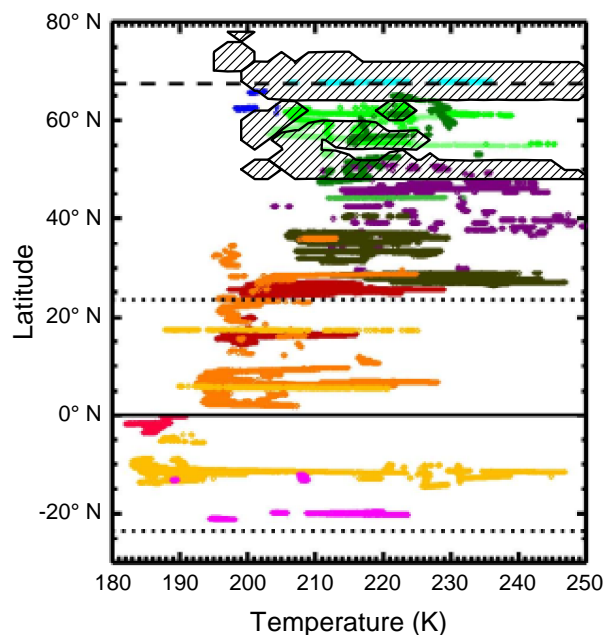
Figure 3. The original of this figure is found in Luebke et al. (2013). It shows the coverage of literature airborne cirrus missions (different colors, legend in the original publication) with respect to latitude and temperature. For this work the figure is adapted to sketch the additional coverage of cirrus measurements during POLSTRACC by a black contour and diagonal stripes.

Since the creation of the original figure by Luebke et al. (2013), the POLSTRACC observations represent the only addition of airborne in situ data at northern polar latitudes. Further observations not included in this figure comprise for example the already mentioned ML-CIRRUS campaign in mid-latitudes (Voigt et al., 2017).

As this study focuses on cirrus at the tropopause, it is worthwhile examining the distribution of cirrus sampling along different tropopause-related vertical coordinates. Different formation pathways and ice particle properties are expected for tropospheric and stratospheric cirrus. The following discussion is limited to observations north of 60° N. Figure 4a displays the cirrus observations in two vertical scales: the abscissa indicates the potential temperature difference d_{TP} of the observation location to the 2 PVU isosurface of potential vorticity (often denoted as dynamical tropopause), which is typically located at a potential temperature of 300 to 320 K (but further ±10 K are possible). The ordinate axis indicates the Brunt-Väisälä frequency N^2 as a measure for the static stability of the atmospheric thermal stratification. The colour coding indicates the temperature as in Fig. 2. Close to the tropopause, roughly linear correlations between d_{TP} and N^2 can be observed, connecting the free, statically less stable troposphere with $N^2 < 2 \cdot 10^{-4}\,\mathrm{s}^{-2}$ to the stratosphere with $N^2 > 4 \cdot 10^{-4}\,\mathrm{s}^{-2}$. This correlation is not compact but spans a corridor with a width of 7 to 10 K. The lower-right branch belongs to January mid-winter measurements, whereas the upper-left branch stems from the March late-winter measurements. This may be interpreted as an increasing stabilization of the tropopause region within two months due to the steady descending motion in the stratosphere. The blue colours

highlight the occurrence of cold cirrus at $T \lesssim 200\,\mathrm{K}$ above the dynamical tropopause. With the latter acting as a transport
barrier for air masses, these cold cirrus on the stratospheric side have in most cases no continuation in the troposphere. These
cirrus delineate the transition to polar stratospheric clouds (PSCs), which do not rely on tropospheric water vapour supply.
Ice nucleation, particle size and habit as well as chemical constitution differ significantly from the tropospheric tropopause
cirrus and they play a crucial role in heterogeneous chemistry in the lowermost stratosphere, impacting especially the budgets
of ozone-depleting substances. Panel b shows the distribution of measurements with respect to N^2. Two major accumulation
regions can be identified, one at 2 to $3 \cdot 10^{-4}\,\mathrm{s}^{-2}$, and another at 4 to $5 \cdot 10^{-4}\,\mathrm{s}^{-2}$. The former can be attributed to tropospheric
cirrus extending up until the thermal tropopause and the latter to stratospheric cirrus with no or only a weak connection to the
troposphere.

The distribution of cirrus observations can also be related directly to potential vorticity (PV) as seen in the bars in Fig. 4c.
As already indicated above, a PV of $2\,\mathrm{PVU}$ is usually chosen as the dynamical tropopause which follows other tropopause
definitions adequately in areas of weak horizontal wind shear, although located systematically below the thermal tropopause
(Gettelman et al., 2011). For the extratropics a value of $3.5\,\mathrm{PVU}$ is often more consistent with the thermal tropopause (Hoinka,
1997). In the figure, the low counts in the 0 to $0.5\,\mathrm{PVU}$ range may suggest a low cloud occurrence in the mid troposphere.
This is not necessarily the case and may be a result of the artificial limitation of the data to temperatures below $235\,\mathrm{K}$, which
has been applied in order to exclude false hits from mixed-phase clouds. So certainly more clouds were encountered there,
composed of either pure ice, mixed phases or liquid water. The highest cirrus occurrence is found below the $2\,\mathrm{PVU}$ isosurface
with a maximum at 1 to $1.5\,\mathrm{PVU}$, which is unambiguously located in the troposphere, where the available water vapour
content is still at least one order of magnitude above stratospheric values. Above, cirrus sampling steadily decreases towards
a rather uniform distribution above the $3.5\,\mathrm{PVU}$ isosurface. This reflects a random distribution of cirrus observations in the
stratosphere, where PV varies strongly in the vertical direction and no single level is preferred for cirrus occurrence. Among
the generally low IWC sampling in the stratosphere, the apparent rise between 6 to $8\,\mathrm{PVU}$ is most likely due to the overall
distribution of flight time in the stratosphere during the campaign, as can be seen by the black line in Fig. 4c.

The following Secs. 4 and 5 focus on one subclass of IWC measurements that represent complete vertical profiles of cirrus
clouds at the tropopause, seen as line-forming dots of data in Fig. 4a.

4 Complete profiles of cirrus at the high latitude tropopause

In order to investigate the radiative impact of cirrus at the tropopause on the profile of temperature and stability, it is necessary
to include the complete profile of the respective cloud in the analysis. The POLSTRACC IWC dataset has been filtered to this
end and a selection of eight events was found that witnessed the required profiles. These events are listed in Tab. 1. There
are some caveats towards the use of the respective cloud profiles. First, very low IWC values at or below about $10\,\mathrm{ppmv}$ are
below the associated water vapour concentrations. These very thin cirrus are common in the Arctic (e.g. Hong and Liu, 2015)
but complicate the distinction of the precise cloud impact in face of the surrounding atmosphere. Second, some profiles are
interrupted by short periods of horizontal flight, extending the time between the cloud bottom and top crossing to well above
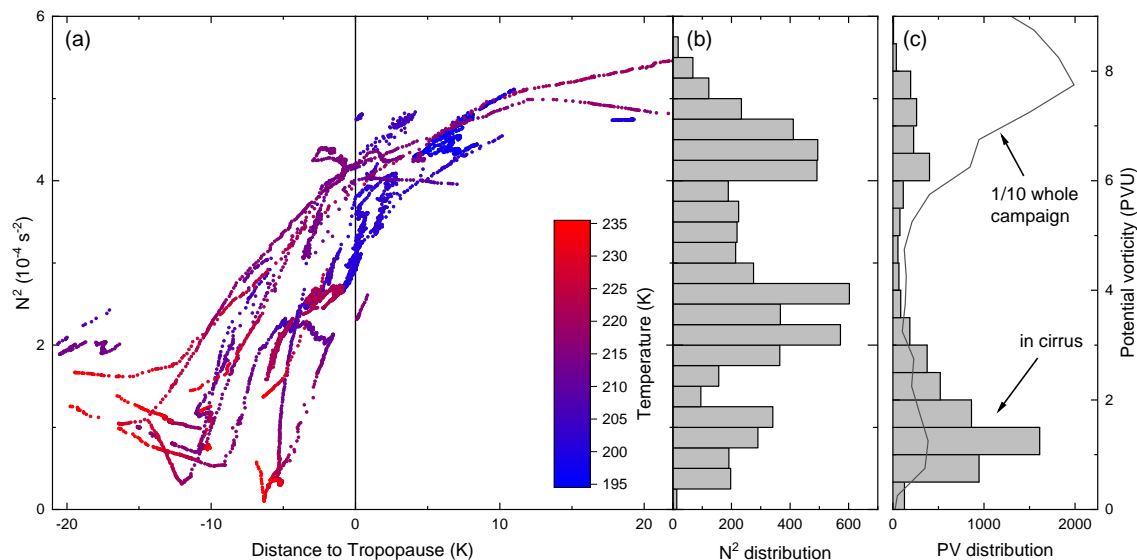
Figure 4. Statistics on the distribution of cirrus sampling below 235 K during POLSTRACC at high latitudes north of 60° N. (a) Distribution over distance to tropopause (given in K of potential temperature) and Brunt-Väisälä frequency N^2. The temperature is indicated in the colour coding. (b) Marginal distribution in N^2. (c) Distribution in potential vorticity. Cirrus sampling in grey bars, and the total flight campaign flight time (divided by 10) in the black line.

Table 1. List of complete cirrus profiles sampled during the POLSTRACC aircraft campaign. The given latitude is an average value for the profile. z denotes the vertical span, T is the temperature range and the maximum IWC is read from the WARAN measurements. The ice water path (IWP) is calculated by integrating the IWC measurements over the whole profile.

Date	Time (UTC)	Lat. (° N)	z (km)	T (K)	max. IWC (ppmv)	IWP (g m^{-2})
13.12.2015	8:12 – 8:33	50.2	8.8 – 12.6	205 – 230	11	1.2
13.12.2015	10:32 – 10:33	51.2	11.3 – 11.8	206 – 208	1	0.04
25.01.2016	12:39 – 13:09	67.8	7.3 – 12.0	201 – 235	43	9.2
31.01.2016	14:29 – 14:41	66.1	3.9 – 8.8	206 – 248	10	4.3
06.03.2016	5:15 – 5:23	67.8	6.8 – 9.7	211 – 230	1	0.3
09.03.2016	14:48 – 14:51	67.2	5.9 – 7.9	219 – 233	51	10.2
18.03.2016	11:09 – 11:14	55.0	10.0 – 11.6	206 – 217	9	0.8
18.03.2016	17:20 – 17:30	50.4	9.6 – 11.1	208 – 218	26	1.5

10 min. This exacerbates the uncertainty as to how well the measurements actually correspond to a real vertical cloud profile. Third, the profiles south of 60° N (Germany, Denmark, southern Sweden) are of lesser interest for this study.

Following these criteria, the profiles on 25 January 2016 and 09 March 2016 are the best candidates for the present study.
210   The January profile still includes two horizontal sections with an accumulated duration of 18 min.

Focusing on these two profiles, Fig. 5a, c display respective time-altitude cross sections (curtains). The cirrus profiles are marked by the thicker section of the shown flight paths in orange. The background shading displays the squared Brunt-Väisälä frequency N^2 from ECMWF reanalysis as an indicator for the vertical static stability of the atmosphere. Troposphere and stratosphere can be clearly distinguished by dark blue colours and greenish/yellow tones, respectively. Troposheric enhance-
215   ments with N^2 up to $4.0\,\mathrm{s}^{-2}$ in the boundary layer and at 5 km altitude are identifiable. The strongest N^2 enhancement is found directly above the thermal tropopause (cyan line, representing the WMO definition), marking a pronounced tropopause inversion layer in both cases, despite very different tropopause altitudes. The extended vertical profiles of the reanalysis data show different patterns in both profiles: On 25 January, the stratospheric profile features a fine-scaled structure of static stability that trigger multiple thermal tropopause identifications (cyan lines). On 09 March instead, one broad stratospheric inversion
220   above 13 km can be seen. Both these observations are not uncommon in regions influenced by orographic gravity waves and in the vicinity of the jet. Missing N^2 data at low altitudes is due to orographic cutoff of the reanalysis data above terrain in Scandinavia or Greenland.

Panels b and d contain the in situ IWC measurements from the WARAN instrument, where the time series are aligned with the curtain plots above. On 25 January, the measurements show a considerable variability in the horizontal flight sections,
225   reflecting the overall patchy atmospheric structure. In contrast, the descent towards the end of the profile is characterised by IWC below 4 ppmv before again enhanced IWC at the cloud bottom below 8.4 km. On 09 March the profile exhibits an almost symmetrical double-peaked structure of IWC distribution inside the cloud. In both cases the IWC varies frequently by up to one order of magnitude. From these slant profiles, we derive vertical IWC profiles for the later sections just by stacking the measurements vertically, neglecting any horizontal inhomogeneity in the clouds. Horizontal flight path sections
230   are condensed into one mean IWC value. Although this no longer represents the actual whole (but unknown) three-dimensional IWC distribution inside the cloud, we deem these artificial one-dimensional profiles still as realistic. Especially in the critical 25 January case, a very similar profile would result if we only considered the last section of the flight path that contains the majority of vertical coverage.

We note that possible lower-level clouds might exist below the observed cirrus or also along ground-reaching flight paths.
235   Beyond possible visual identification, such clouds were excluded from sampling (through inlet flow cutoff) during the POL-STRACC campaign to avoid impairment of the targeted measurements of low concentrations of water vapour and cloud water in the upper troposphere and above.

5   Radiative transfer calculations

Radiative transfer calculations focus on selected ice clouds that have been probed during the POLSTRACC flights on 25
240   January 2016 and 09 March 2016. The ice clouds on these days show significantly different geometrical thicknesses and different shapes of the profiles of the ice water content (IWC(z)) (Fig. 6). It is shown how the clouds affect the radiation
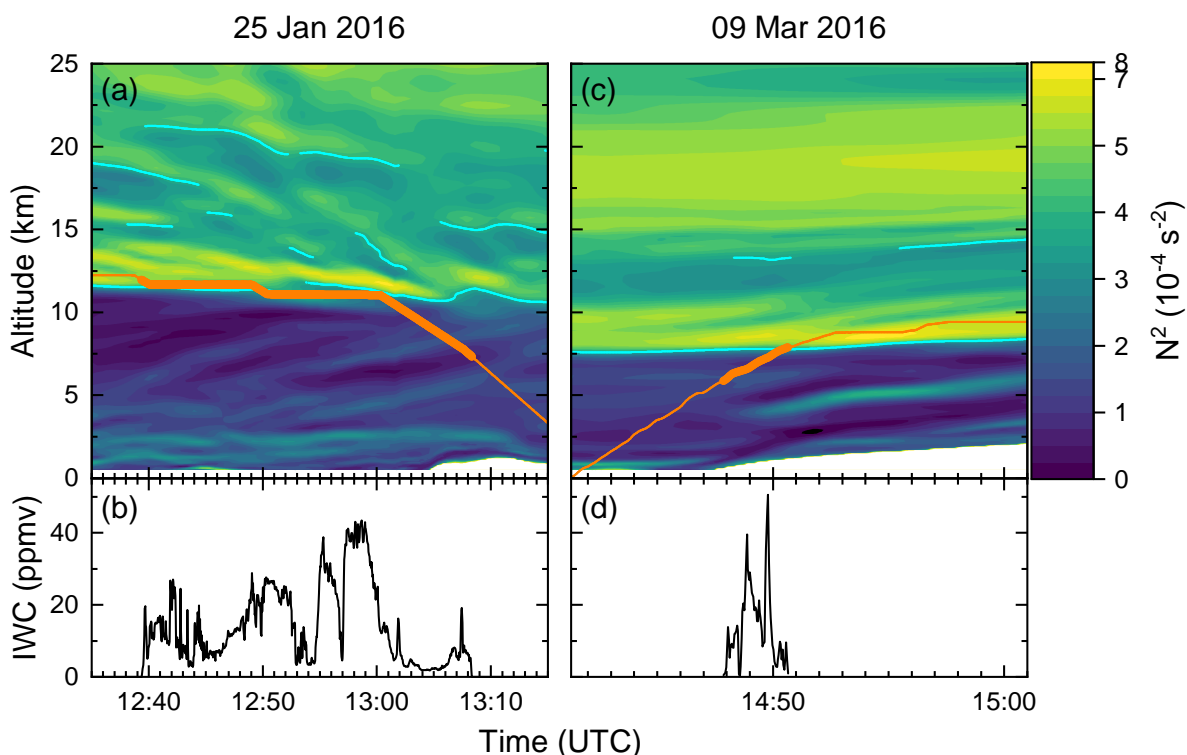
Figure 5. Time series of the cirrus cloud profiles on 25 January and 09 March 2016. (a) and (c) The orange line indicates the aircraft flight path. The thicker section highlights the location of the cloud profile. The background shading displays a vertical cross section of squared Brunt-Väisälä frequency N^2 from ECMWF reanalysis data interpolated along the flight track. Cyan lines indicate thermal tropopause altitudes according to the WMO definition. (b) and (d) Time series of IWC measurements from the WARAN instrument.

budget at the top and at the bottom of the atmosphere (TOA, BOA) as well as the profiles of the heating rate. Since the profiles $IWC(z)$ reveal vertical fine structures, one further goal was to estimate the effects these structures could have on the radiation parameters. According to conditions at Arctic latitudes radiative transfer simulations were carried out for large solar zenith angles (sza) and for atmospheres over surfaces covered by snow of different age, over mixed surfaces, and over an ice free ocean.

The mentioned uncertainty with the IWC measurements, likely an underestimation, is addressed by repeated calculations using the IWC profiles times 5. The differences in the results are mainly discussed in the scope of TOA net irradiances. Concerning the results for other quantities, we refer to the appendix of the manuscript.
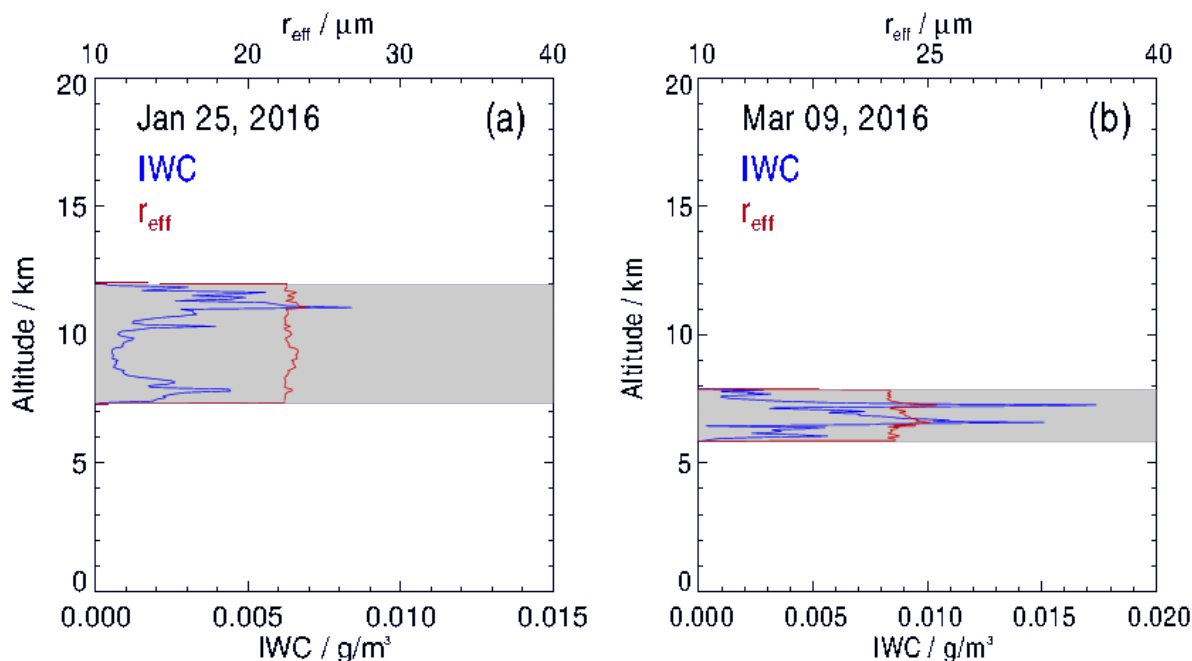
Figure 6. Vertical profiles of the measured ice water content IWC on (a) 25 January and (b) 09 March 2016 (blue curves) and the effective radius r_{eff} (red curves) derived from a parametrization after Liou et al. (2008) describing r_{eff} as a function of IWC. Grey shading illustrates the total vertical extent of the measured ice clouds.

5.1 Methods

5.1.1 Radiative transfer model and input parameters

Radiative transfer calculations are based on the routine UVSPEC from the program package libRadtran (Mayer and Kylling, 2005). The 1D model provides static profiles of irradiances and heating rates in the shortwave (SW = $0.4 - 4.0\,\mu$m) and the longwave spectral range (LW = $4.0 - 100\,\mu$m). Figure 6 shows IWC profiles measured on 25 January 2016 and on 09 March 2016. Apart from the IWC, radiative transfer calculations need the effective radius (r_{eff}) as input. While the IWC is based on in situ measurements, assumptions are made for the r_{eff}. The vertical profiles $r_{eff}(z)$ have been generated by using a parameterization after Liou et al. (2008) which allows to describe r_{eff} as a function of the IWC at Arctic latitudes (Fig. 6).

After Liou et al. (2008), the dependence of r_{eff} on IWC is only weak. Consequently, Fig. 6 shows relatively small altitude dependent variations of the r_{eff} and similarly, r_{eff} changes by less than a factor 2 with IWC times 5. Thus, the vertical profile of the ice cloud optical thickness is only highly correlated with the profile of the IWC itself.

The translation of IWC and r_{eff} into the optical properties follows Baum et al. (2005, 2007). Due to the lack of in situ measurements of ice crystal habits during POLSTRACC the UVSPEC setting of a general habit mixture (GHM) is taken. The GHM assumes size-dependent fractions of different habits including for example pristine crystals like droxtals, columns and
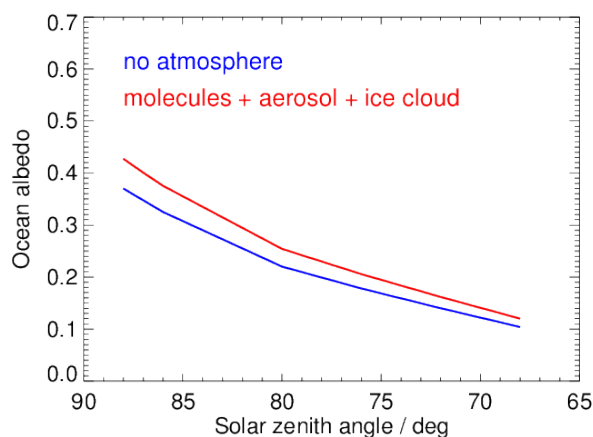
Figure 7. Broadband albedo at the ocean surface as a function of solar zenith angle after Payne (1972) for an atmospheric transmission transmission of 1.0 (blue curve) and for the atmosphere on 25 January 2016 containing molecules, aerosol particles, and an ice cloud (red curve).

plates, bullet rosettes as well as aggregates of columns and plates. Under these assumptions the optical thickness of the ice cloud on 25 January 2016 results in $\tau_{0.55\,\mu m} = 0.65$ and in $\tau_{0.55\,\mu m} = 0.68$ for the ice cloud on 09 March 2016. Horizontally homogeneous model clouds are resolved vertically into 72 layers in order to adequately represent measured IWC fine structures.

Concerning the reflection properties of the lower boundary, surface types typical for Arctic regions are considered: a snow/ice free ocean, a snow-covered surface and land surfaces composed of snow-covered and snow-free areas. In principal, the albedo (α) of these surface types is highly variable in time and space and depends on various parameters. The ocean albedo, for example, is affected by the surface wind speed and by the type and concentration of existing hydrosols. The snow albedo depends on the grain size of the snow, its age, and the degree of pollution. Since the surface albedo is defined as the ratio of the upward to the downward directed irradiance (Eq. 5) it is also a function of the actual atmospheric optical thickness determining the ratio of downward direct and diffuse radiation.

Simplifications are made for numerical simulations. In case of the ocean, a broadband albedo following measurements of Payne (1972) is used which depends on the solar zenith angle (sza) and represents a mean surface roughness at $7.5\,\mathrm{kn}$ ($3.9\,\mathrm{m\,s^{-1}}$) windspeed. The ocean albedo increases significantly for large sza values (Fig. 7). As an approximation the snow surface is represented by a constant broadband albedo of $\alpha_{\mathrm{snow\ 1}} = 0.60$ and $\alpha_{\mathrm{snow\ 2}} = 0.85$, representing old and fresh snow, respectively (e.g. Gardner and Sharp, 2010). Since the variation of the snow albedo is less pronounced for sza $\geq 60°$ compared to the ocean albedo, a sza-dependence is not taken into account. Furthermore, to estimate albedo effects of Arctic land surfaces that are composed of different components, as for example a mixture of snow and snow-free (rocky) areas, the constant values $\alpha_{\mathrm{mix\ 1}} = 0.15$ and $\alpha_{\mathrm{mix\ 2}} = 0.30$ are used. In the LW range a constant emissivity of $\epsilon = 1.0$ is assumed for all surface types.

For the aerosol a UVSPEC setting is selected which describes a standard maritime haze in the lower $2\,\mathrm{km}$ in the winter season. The vertical profiles of the meteorological parameters and the trace gases are described in the following section.

5.1.2 Meteorological data and trace gases

In situ values of meteorological quantities like atmospheric pressure and temperature as well as geolocation are provided by the Basic HALO Measurement And Sensor System (BAHAMAS) at a 1 Hz frequency (Giez et al., 2017). For the one-dimensional radiative transfer calculations, a complete profile of temperature and radiatively relevant species in the troposphere and stratosphere is required. We therefore use data from the European Centre for Medium-Range Weather Forecasts Integrated Forecast System (ECMWF IFS) analysis product. Distributions of methane (CH_4), nitrogen monoxide (NO) and nitrogen dioxide (NO_2) are taken from the Copernicus Atmospheric Monitoring Service (CAMS). The ozone (O_3) distribution is taken from the Global and regional Earth-system Monitoring using Satellite and in situ data (GEMS). High resolution hourly data on 137 model levels are provided for the meteorological quantities including specific humidity (3-hourly and 60 levels for CAMS/GEMS). The model data are interpolated in space and time on the flight paths of the HALO aircraft during the POLSTRACC campaign.

In order to assess the consistency of the model with the in situ data, we performed a comparison of the aircraft measurements and interpolated model values for temperature, specific humidity (water vapour) and ozone during the relevant flight sections. Temperature is captured quite well by the model, with a slight tendency to underestimate the values by up to 2 K. The vertical structure in (slant) profiles is consistent, especially the height of the thermal tropopause coincides from both sources. This also translates to a good representation of specific humidity. The GEMS ozone product is consistent with the in situ measurements from the on-board FAIRO instrument (Zahn et al., 2012) near the surface and for the most part in the stratosphere. In the regime above 500 ppbv O_3, the model does not capture the small scale variability of the observations with typical deviations of 15 to 20 %.

5.1.3 Radiative quantities

With a view to the following sections the definitions of six radiative quantities are given. A basic model output is the upward and downward directed irradiance ($I_{up,\Delta\lambda}$, $I_{down,\Delta\lambda}$) at each model layer. These irradiances are integrated over a wavelength interval $\Delta\lambda$, here over the SW and LW range, and are given in Wm^{-2}. Their sum is the balance of incoming and outgoing radiation at each model layer:

$$I_{\Delta\lambda} = I_{down,\Delta\lambda} + I_{up,\Delta\lambda} \; . \tag{4}$$

Note, the sign of the upward directed irradiances $I_{up,\Delta\lambda}$ is negative, downward directed irradiances $I_{down,\Delta\lambda}$ are defined as positive.

The absolute value of the ratio of the upward to the downward directed irradiance defines the albedo α in the wavelength interval $\Delta\lambda$:

$$\alpha_{\Delta\lambda} = |(I_{up,\Delta\lambda}/I_{down,\Delta\lambda})| \; . \tag{5}$$

Balancing the irradiances $I_{\Delta\lambda}$ over the SW and LW spectral intervals gives the net radiation budget or net irradiance in $\mathrm{Wm^{-2}}$, hereinafter referred to as F_{net}:

$$F_{\mathrm{net}} = I_{\mathrm{SW}} + I_{\mathrm{LW}} \ . \tag{6}$$

The net forcing $\mathrm{RF_{net}}$ in $\mathrm{Wm^{-2}}$ is defined as the difference of F_{net} calculated for the atmosphere with an embedded ice cloud minus F_{net} for the cloud free atmosphere:

$$\mathrm{RF_{net}} = F_{\mathrm{net,icecloud}} - F_{\mathrm{net,cloudfree}} \ . \tag{7}$$

The heating rate $H_{\Delta\lambda}$ integrated over the wavelength interval $\Delta\lambda$ describes the temperature change of a model layer in $\mathrm{Kd^{-1}}$ (Kelvin per day) and is defined as:

$$H_{\Delta\lambda} = -1/(\rho_{\mathrm{air}}\, c_p) \cdot \partial I_{\Delta\lambda}/\partial z \ . \tag{8}$$

ρ_{air} denotes the air density, c_p the specific heat capacity of air at constant pressure. $\partial I_{\Delta\lambda}/\partial z$ is the vertical divergence of the irradiance $I_{\Delta\lambda}$.

Balancing $H_{\Delta\lambda}$ over the SW and LW spectral interval gives the net heating rate in $\mathrm{Kd^{-1}}$, hereinafter referred to as H_{net}:

$$H_{\mathrm{net}} = H_{\mathrm{SW}} + H_{\mathrm{LW}} \ . \tag{9}$$

5.2 Results

5.2.1 TOA net irradiances

Net irradiances at the TOA ($F_{\mathrm{net,TOA}}$) as a function of the sza based on IWC profiles measured on 25 January and on 09 March 2016 are shown in Fig. 8. Solar zenith angles in the range of $88° \geq \mathrm{sza} \geq 60°$ occur at Arctic latitudes north of $66°\,\mathrm{N}$ within the period from 10 September to 31 March. Figure 8a compares $F_{\mathrm{net,TOA}}$ over an ice-free ocean and over surfaces assumed to be covered with aged ($\alpha_{\mathrm{snow\ 1}} = 0.60$) and fresh snow ($\alpha_{\mathrm{snow\ 2}} = 0.85$). In Fig. 8b results for an ocean surface are replaced by those for mixed land surfaces described by the albedo values $\alpha_{\mathrm{mix\ 1}} = 0.15$ and $\alpha_{\mathrm{mix\ 2}} = 0.30$.

Looking at the curves of $F_{\mathrm{net,TOA}}$ in Fig. 8, for all surface albedo values, the net irradiance at the TOA is minimal at highest sza and increases with decreasing sza. Whilst becoming positive for an ocean or mixed snow surface, it remains negative for fresh and highly reflecting snow surfaces in the shown sza range (Fig. 8a, b). This already points to the strong impact of surface albedo on the radiation budget.

In Fig. 8a, although at the maximum sza = $88°$ the difference between $F_{\mathrm{net,TOA}}$ over the ocean and $F_{\mathrm{net,TOA}}$ over the snow surfaces is relatively small, e.g. $10.2\,\mathrm{Wm^{-2}}$ for $\alpha_{\mathrm{ocean}} = 0.37$ and $\alpha_{\mathrm{snow}} = 0.85$ on 25 January 2016, the curves diverge quickly with decreasing sza. Reason is that in the case of atmospheres containing semi-transparent ice clouds or under cloud-free conditions, the contribution of the (positive) sum of downward and upward directed solar irradiance at the TOA increases with decreasing surface albedo and with decreasing sza. This effect is further enhanced by differences between the ocean and the constant snow albedo which increase with decreasing sza. Furthermore, the transition from negative to positive values of
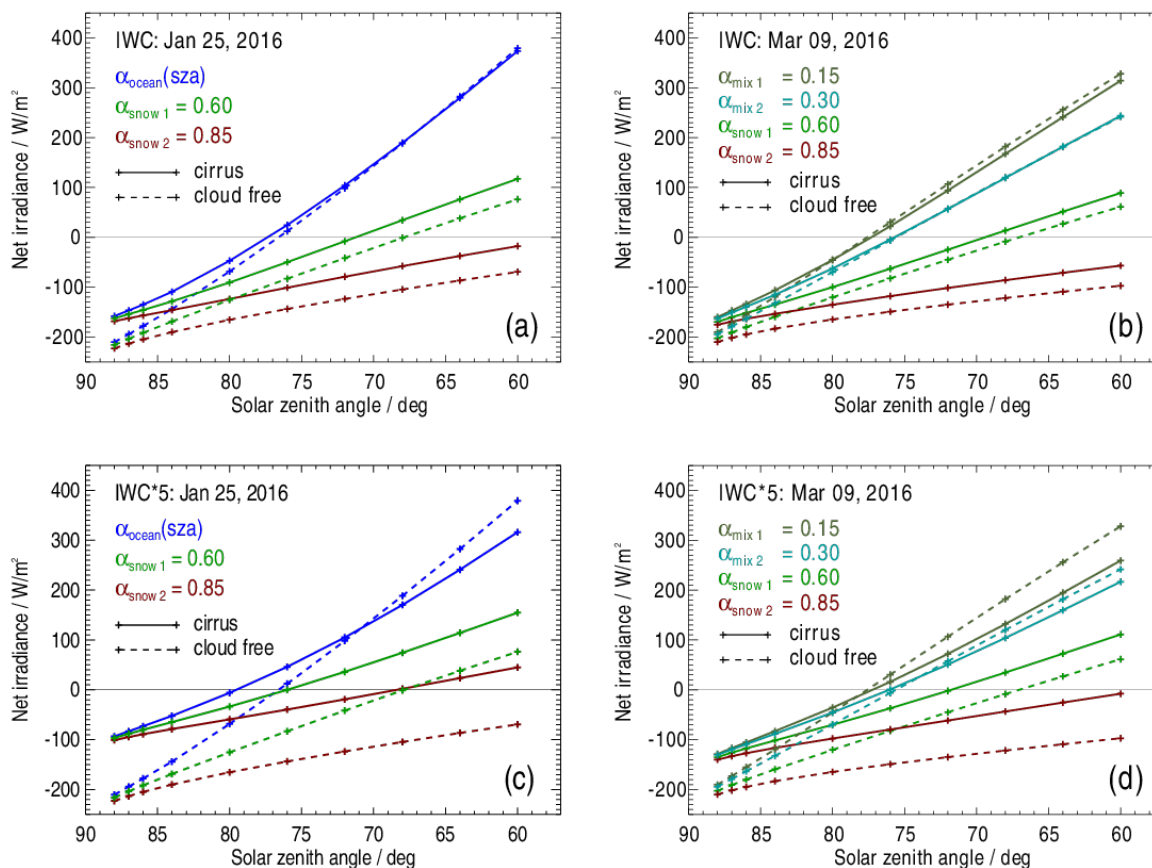
Atmospheric
Chemistry
and Physics
Discussions
Open Access
EGU

Figure 8. (a) Net irradiances at the top of the atmosphere on 25 January 2016 as a function of solar zenith angle over an ice-free ocean and over snow-covered surfaces with albedo values as indicated. (b) As in (a), but for the atmosphere on 09 March 2016 and with the ocean albedo replaced by values assumed for mixed surfaces. Solid curves result for the atmosphere with an embedded ice cloud, dashed curves for the same but cloud free atmosphere. (c) and (d) as in (a) and (b), but for ice clouds with higher optical thicknesses obtained by multiplying the measured profile IWC(z) with a factor of 5.

$F_{\mathrm{net,TOA}}$, equivalent to a change from a loss to a gain of radiative energy, occurs at a greater sza over the ocean than over

345   aged snow ($\alpha_{\mathrm{snow\,1}} = 0.60$, Fig. 8a). In case of fresh snow ($\alpha_{\mathrm{snow\,2}} = 0.85$) $F_{\mathrm{net,TOA}}$ remains negative in the entire range $88° \geq$ sza $\geq 60°$ (Fig. 8a, b). Figure 8b presents results for 09 March 2016, i.e. curves for $\alpha_{\mathrm{mix\,1}} = 0.15$ and $\alpha_{\mathrm{mix\,2}} = 0.30$ instead of those for the ocean albedo. As to be expected, their behaviour as a function of sza and in relation to the results gained for snow surfaces is qualitatively the same as in Fig. 8a. In case of $\alpha_{\mathrm{mix\,2}}$ the differences of $F_{\mathrm{net,TOA}}$ between the cloud-free atmosphere and the atmosphere containing an ice cloud are smallest for sza $\leq 75°$. This is a constellation where the specific

350   ice cloud properties result in a negligible net radiative forcing $\mathrm{RF_{net}}$ (Eq. 7). $\mathrm{RF_{net}}$ curves are shown and further discussed in Sec. 5.2.3.

Atmospheric
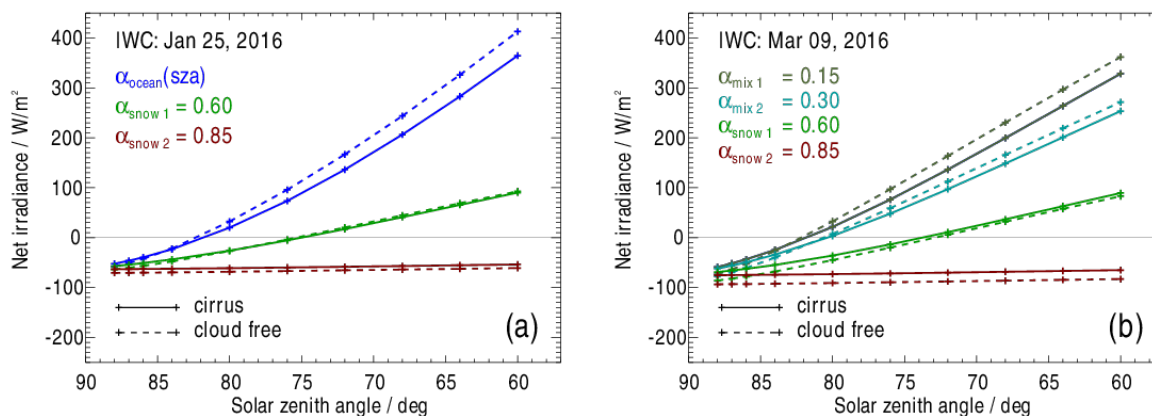Chemistry
and Physics
Discussions

Figure 9. Net irradiances at the bottom of the atmosphere (surface), otherwise as in Fig. 8.

It was also investigated to what extent higher optical thicknesses of the ice clouds affect $F_{\mathrm{net,TOA}}$. For this purpose measured profiles IWC(z) were multiplied by a factor of 5, resulting in optical thicknesses of $\tau_{0.55\,\mu\mathrm{m}} = 0.65 = 2.94$ and $\tau_{0.55\,\mu\mathrm{m}} = 0.65$ = 2.85 for 25 January and 09 March, respectively. In the SW, higher optical thicknesses of the ice clouds lead to a larger

355 contribution of the upward directed reflected radiation to $F_{\mathrm{net,TOA,SW}}$. At the same time the contribution of the LW emission to $F_{\mathrm{net,TOA,LW}}$ is reduced, since the low temperatures of the ice cloud layers are accompanied with higher emissivities in case of increased optical thicknesses (Figs. 8c, d vs. Figs. 8a, b). One net effect is an overall shift of $F_{\mathrm{net,TOA}}$ towards higher values, especially noticeable at large sza, where SW effects are increasingly negligible. For example, $F_{\mathrm{net,TOA}}$ is increased by about $65\,\mathrm{Wm}^{-2}$ on 25 January and by about $45\,\mathrm{Wm}^{-2}$ on 09 March at sza = 88°. Furthermore, comparing Figs. 8c, d with Figs. 8a,

360 b, the curves are closer together, because the higher optical thicknesses of the ice clouds dampen the effect of different surface albedo values on $F_{\mathrm{net,TOA}}$. Ultimately, increasing IWC(z) leads to a transition from negative to positive $F_{\mathrm{net,TOA}}$ occuring at all (25 January, sza $\leq$ 68°, $\alpha_{\mathrm{snow\ 2}} = 0.85$) or to a transition that is shifted towards larger sza when compared to the curves in Figs. 8a, b.

5.2.2 Surface net irradiances and surface albedo

365 Figure 9 presents net irradiances at the surface, or bottom of the atmosphere, $F_{\mathrm{net,BOA}}$. The effect of various surface albedo values on the relative course of the curves to each other corresponds to that in Fig. 8. However, in comparison to $F_{\mathrm{net,TOA}}$ (Fig. 8) the decrease in $F_{\mathrm{net,BOA}}$ with increasing sza is less pronounced. Reason is the diffuse component of incident solar radiation at the surface which attenuates the sza dependence of the total (direct plus diffuse) downward directed irradiance. In case of $\alpha_{\mathrm{snow\ 2}} = 0.85$ multiple scattering processes between surface and atmosphere further enhance such an effect leading

370 to an extremely weak dependence of the $F_{\mathrm{net,BOA}}$ on sza. Finally, the ice cloud reduces downward directed net irradiances (positive irradiances) at the ocean surface within the range 83° $\geq$ sza $\geq$ 60° on 25 January 2016, when compared to the cloud
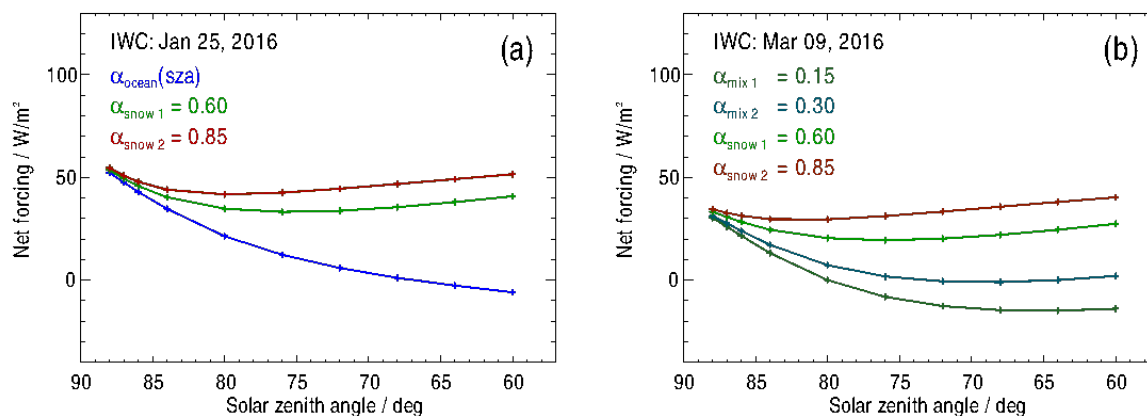
Figure 10. TOA net radiative forcings as a function of the solar zenith angle on (a) 25 January 2016 and on (b) 09 March 2016 for different surface albedo assumptions as indicated.

free atmosphere. Over a bright snow surface with $\alpha_{\text{snow 2}} = 0.85$ the existence of an ice cloud decreases upward directed net irradiances. For $F_{\text{net,BOA}}$ with IWC times 5, see Fig. A1.

5.2.3 Radiative forcing

375 Net radiative forcings at the TOA ($\text{RF}_{\text{net,TOA}}$) as defined by Eq. 7, are again displayed as a function of sza for 25 January 2016 and 09 March 2016 in Fig. 10a, b. Over bright snow surfaces $\text{RF}_{\text{net,TOA}}$ is positive on both days within the range 88° $\geq$ sza $\geq$ 60°. In other words, the model ice clouds cause an energy gain of the earth-atmosphere system. Over the ocean, positive $\text{RF}_{\text{net,TOA}}$ result for large sza values. With decreasing sza, however, $\text{RF}_{\text{net,TOA}}$ becomes smaller and even turns into the negative range. This again is due to the fact that at a large sza the ocean albedo is high, but decreases significantly with

380 decreasing sza (Fig. 7). Over a bright ocean ice clouds reduce outgoing radiation, whereas they increase it over a dark ocean. The higher the optical thickness of the ice cloud, the larger is the sza at which the transition to a negative $\text{RF}_{\text{net,TOA}}$ occurs. Due to the higher optical thickness of the ice cloud on 09 March 2016 compared to that on 25 January 2016 (Sec. 5.1.1), $\text{RF}_{\text{net,TOA}}$ on 09 March is shifted towards smaller values as shown by the curves for $\alpha_{\text{snow 1}} = 0.60$ and $\alpha_{\text{snow 2}} = 0.85$ in Fig. 10a and b. For $\text{RF}_{\text{net,TOA}}$ with IWC times 5, see Fig. A2.

385 5.2.4 IWC fine structures

IWC profiles measured during the POLSTRACC campaign show vertical fine structures (e.g. Fig. 6a, b). It is investigated how such structures affect the profiles of the net irradiances F_{net} and heating rates $H(z)$. As a reference, additional radiative transfer calculations have been carried out for synthetic ice clouds with a vertically constant profile $\text{IWC}(z)_{\text{const}}$. Profiles $\text{IWC}(z)_{\text{const}}$ together with the assigned profiles of the effective radius $r_{\text{eff}}(z, \text{IWC}(z))$ after Liou et al. (2008) are designed

390 in such a way that the optical thickness remains the same as for $\text{IWC}(z)_{\text{meas}}$. Profiles of the temperature and the ice water
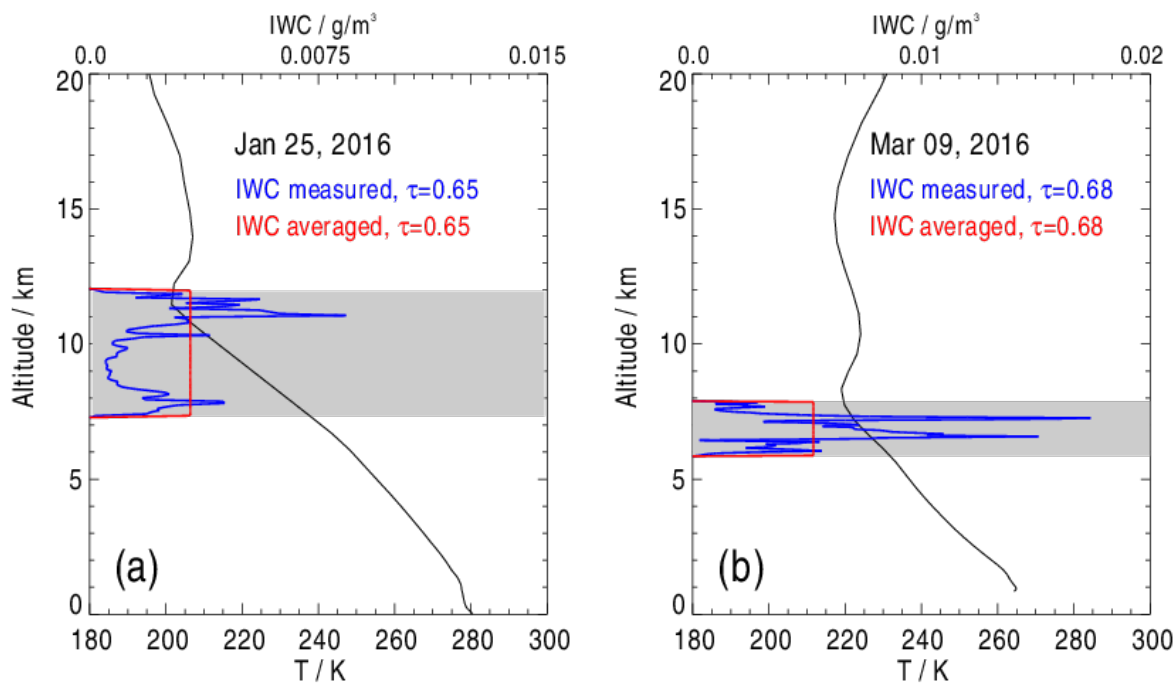
Figure 11. Vertical profiles of temperature (black curve), measured IWC (blue curve), and a vertically constant IWC resulting in the same cloud optical thickness as the measured IWC (red curve) for (a) 25 January 2016 and (b) 09 March 2016. τ denotes the ice cloud optical thickness at 0.55 μm. Grey shading illustrates the total vertical extent of the ice clouds.

contents $IWC(z)_{meas}$ and $IWC(z)_{const}$ for 25 January 2016 and 09 March 2016 are presented in Fig. 11. On 25 January 2016 $IWC(z)_{meas}$ is vertically extended (7.3 – 12.0 km) and shows a pronounced maximum in the upper third between about 11 km and 12 km altitude and a second peak near the cloud base between about 7.2 km and 8.2 km (Fig. 11a). On 09 March 2016 $IWC(z)_{meas}$ is confined to a smaller altitude range (5.9 – 7.9 km) with maximum IWC values in the middle of the cloud layer.

395   Figures 12a, d, g, j compare SW and LW irradiance profiles, I_{SW} and I_{LW}, obtained for the profiles $IWC(z)_{meas}$ and $IWC(z)_{const}$. Differences between SW and LW irradiances follow the altitude-dependent difference between measured and constant IWC profiles. Note, apart from the influence of trace gases and aerosols and in view of a rather weak variability of the profiles of the effective radius (Fig. 6), the LW thermal emission of a layer is proportional to the ice water content, and herewith proportional to the cloud optical thickness. In addition, the LW emission depends on the temperature distribution within the ice

400   cloud layer. At the large solar zenith angle sza = 88° LW radiation dominates the altitude-dependent changes in the irradiance profiles (Fig. 12a, g).

On 25 January 2016 upward directed (negative) LW irradiances (I_{LW}) at the cloud top are smaller for the measured profile $IWC(z)_{meas}$ when compared to $IWC(z)_{const}$ (Fig. 12a). Reason is a smaller LW emission from the IWC maximum near the cloud top due to relatively cold temperatures in combination with an increased optical thickness at these layers. Below the

405   upper IWC peak, upward directed LW irradiances for $IWC(z)_{meas}$ are larger than for $IWC(z)_{const}$ because the upward directed

emission from the surface and from the IWC maximum near the cloud base are balanced with smaller downward directed (positive) emissions from the colder layers above. Major differences between irradiances for the measured and constant IWC profile are confined to the layers within the cloud and reach up to about $5 \, \mathrm{Wm^{-2}}$. Thus on 25 January 2016, it is the combination of the vertical inhomogeneity of the IWC profile (two different maxima) and the geometrical thickness of the entire ice cloud

410 associated with larger vertical temperature differences that cause pronounced altitude dependent LW irradiance differences. Here, the ice cloud causes irradiance differences in the order of a few $\mathrm{Wm^{-2}}$ which penetrate up to the TOA (see Tab. 2).

On 09 March 2016 the geometrical thickness of the ice cloud is reduced showing two closely spaced maxima in the middle of the IWC profile. The overall shape is more symmetric than on 25 January 2016 (Fig. 11b). Switching from the measured to the constant IWC profile does not lead to a stronger weighting of layers emitting LW radiation with significantly different

415 temperatures. As a consequence, LW irradiance differences inside the ice cloud are smaller than on 25 January 2016 (about $2 \, \mathrm{Wm^{-2}}$) and even smaller at the TOA and BOA (Fig. 12g; Tab. 2).

A smaller solar zenith angle of sza = 72° increases the contribution of SW radiation significantly (Fig. 12d, j). Irradiance differences due to the influence of differently shaped IWC profiles are mainly a result of scattering processes. SW downward directed (positive) irradiances calculated for $\mathrm{IWC}(z)_{\mathrm{meas}}$ are smaller below the relative IWC maxima due to shadowing effects

420 (Fig. 12d, j) which are negligible in case of $\mathrm{IWC}(z)_{\mathrm{const}}$. On 25 January 2016 the vertically extended maximum of the IWC produces greatest differences. Small enhancements of downward directed SW irradiances result for $\mathrm{IWC}(z)_{\mathrm{meas}}$ at the upper edge of the maxima due to multiple scattering effects (Fig. 12j).

Figures 12b, e, h, k compare profiles of net irradiances $F_{\mathrm{net}}(z)$ balanced over the SW and LW range based on $\mathrm{IWC}(z)_{\mathrm{meas}}$ and $\mathrm{IWC}(z)_{\mathrm{const}}$. As is to be expected, $F_{\mathrm{net}}(z)$ reflects that the specific properties of the profile $\mathrm{IWC}(z)_{\mathrm{meas}}$ on 25 January

425 2016 cause greatest differences to the results obtained for $\mathrm{IWC}(z)_{\mathrm{const}}$. Table 2 contains data of $F_{\mathrm{net}}(\mathrm{IWC}(z)_{\mathrm{meas}})$ and $F_{\mathrm{net}}(\mathrm{IWC}(z)_{\mathrm{const}})$ as well as their differences $\Delta F_{\mathrm{net}} = F_{\mathrm{net}}(\mathrm{IWC}(z)_{\mathrm{meas}}) - F_{\mathrm{net}}(\mathrm{IWC}(z)_{\mathrm{const}})$ at the TOA and at the BOA. Numbers show that for the individual day $\Delta F_{\mathrm{net,TOA}}$ and $\Delta F_{\mathrm{net,BOA}}$ are of the same order of magnitude independent of the two surface types considered here. In most cases absolute values of ΔF_{net} are smaller than $1 \, \mathrm{Wm^{-2}}$. An exception are again the results for 25 January 2016 at TOA. The reason is already given by Fig. 12a, d showing that at cloud top upward

430 directed (negative) LW irradiances obtained for $\mathrm{IWC}(z)_{\mathrm{const}}$ are about $2.5 \, \mathrm{Wm^{-2}}$ larger than those obtained for the profile $\mathrm{IWC}(z)_{\mathrm{meas}}$. For results with IWC times 5, see Tab. A1.

5.2.5 Heating rates

According to Eq. 8 wavelength integrated net heating rate profiles are proportional to the vertical divergence of the net irradiance $\partial F_{\mathrm{net}}(z)/\partial z$ and can be read from the profiles shown in Fig. 12b, e, h, k. $\partial F_{\mathrm{net}}(z)/\partial z$ is mainly affected by the profile

435 of $\mathrm{IWC}(z)$ within the ice cloud, so that their differences due to $\mathrm{IWC}(z)_{\mathrm{meas}}$ and $\mathrm{IWC}(z)_{\mathrm{const}}$ are particularly pronounced there and are minimal above and below the cloud layer. As a consequence, differences in net heating rate profiles $\Delta H_{\mathrm{net}}(z)$ associated with $\mathrm{IWC}(z)_{\mathrm{meas}}$ and $\mathrm{IWC}(z)_{\mathrm{const}}$ occur within the ice cloud on both days, 25 January, and 09 March 2016, and for both solar zenith angles sza = 88° and sza = 72° (Fig. 12c, f, j, l). On 25 January 2016 the maximum ΔH_{net} is $4.47 \, \mathrm{Kd^{-1}}$ at sza = 72° whereas the minimum ΔH_{net} results in $-1.18 \, \mathrm{Kd^{-1}}$ at sza = 88°. On 09 March 2016 corresponding maximum and
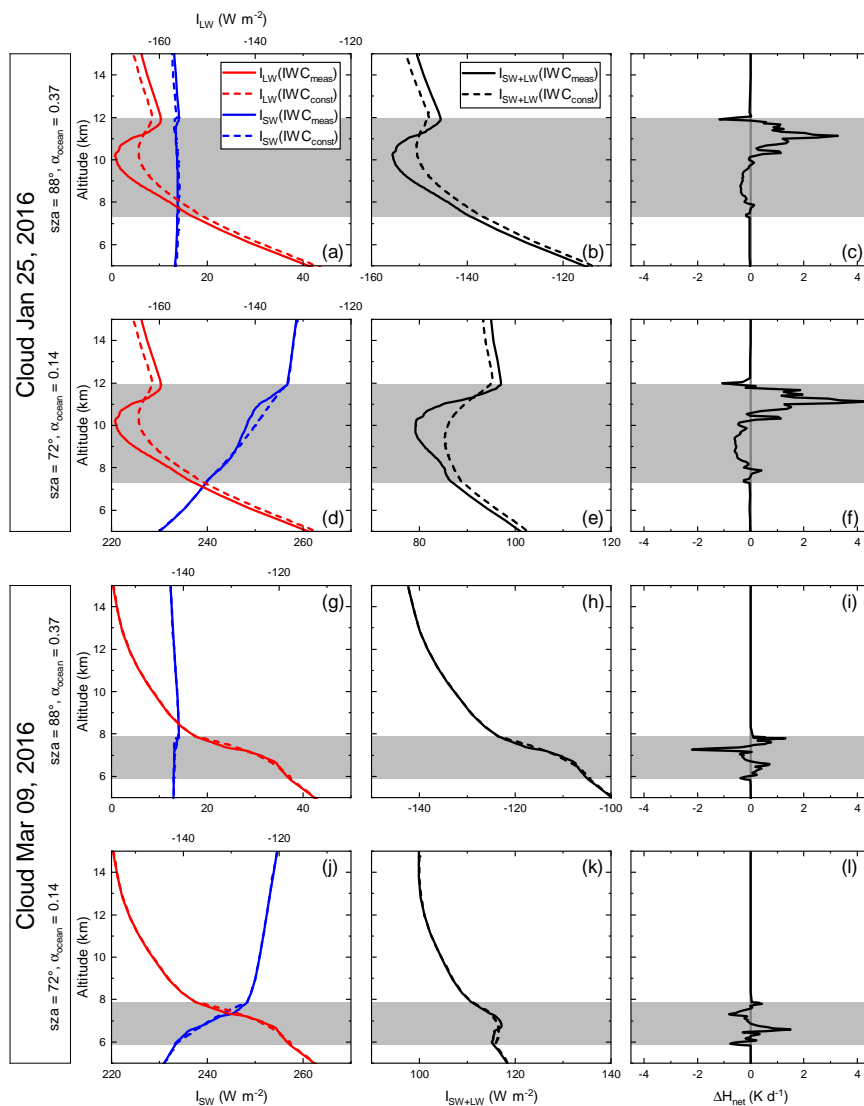
Figure 12. Irradiance profiles of measured (solid) and constant (dashed) IWC profiles for selected values of solar zenith angle and albedo as indicated. Left column: net LW (red, top axis scale) and SW (blue, bottom axis scale) irradiances. Centre column: net irradiances. All irradiance scales span a range of $50\,\mathrm{W\,m^{-2}}$, albeit at different absolute positions. Right column: Difference of the net heating rate profile between the measured and the constant IWC profile.

440 minimum values are $1.50\,\mathrm{K\,d^{-1}}$ and $-2.20\,\mathrm{K\,d^{-1}}$, respectively. Within the cloud, ΔH_{net} is in the order of magnitude of the net heating rate $H_{\mathrm{net}}(z)$, whereas above and below the cloud $\Delta H_{\mathrm{net}}(z)$ is negligible.

Figure 12 presents curves that result for an ocean surface as the lower boundary. Comparing heating rate differences $\Delta H_{\mathrm{net}} = H_{\mathrm{net}}(\mathrm{IWC_{meas}}) - H_{\mathrm{net}}(\mathrm{IWC_{const}})$ over the ocean with those over snow ($\alpha_{\mathrm{snow\,2}} = 0.85$) reveals a difference of

Atmospheric
Chemistry
and Physics
Discussions

Open Access

EGU

Table 2. Net irradiances at the top of the atmosphere and at the surface, $F_{\text{net,TOA}}$ and $F_{\text{net,BOA}}$, calculated for measured and vertically constant profiles of the ice water content ($\text{IWC}(z)_{\text{meas}}$ and $\text{IWC}(z)_{\text{const}}$). ΔF_{net} is the difference $F_{\text{net}}(\text{IWC}_{\text{meas}})$ minus $F_{\text{net}}(\text{IWC}_{\text{const}})$. Selected are results for four solar zenith angles (sza) and for the days 25 January 2016 and 09 March 2016.

Date	sza	$F_{\text{net,TOA}}$ / $F_{\text{net,BOA}}$ for $\text{IWC}(z)_{\text{meas}}$	$F_{\text{net,TOA}}$ / $F_{\text{net,BOA}}$ for $\text{IWC}(z)_{\text{const}}$	$\Delta F_{\text{net,TOA}}$ / $\Delta F_{\text{net,BOA}}$ (measured - constant)
	(°)	(Wm^{-2})	(Wm^{-2})	(Wm^{-2})
α_{ocean} (sza)				
25 Jan 2016	88	-157.96 / -52.34	-160.80 / -51.63	2.84 / -0.71
25 Jan 2016	80	-47.06 / 20.04	-49.30 / 20.51	2.24 / -0.36
25 Jan 2016	72	103.99 / 136.18	101.74 / 136.65	2.25 / -0.47
25 Jan 2016	64	279,63 / 282.95	277.37 / 283.42	2.26 / -0.47
09 Mar 2016	88	-164.38 / -63.66	-164.34 / -63.53	-0.04 / -0.13
09 Mar 2016	80	-53.29 / 13.12	-53.27 / 13.27	-0.02 / -0.15
09 Mar 2016	72	96.23 / 138.83	96.28 / 138.97	-0.05 / -0.14
09 Mar 2016	64	272.11 / 296.81	272.17 / 296.94	-0.06 / -0.13
$\alpha_{\text{snow}} = 0.85$				
25 Jan 2016	88	-168.17 / -62.19	-171.89 / -62.66	3.72 / -0.53
25 Jan 2016	80	-123.63 / -61.21	-125.83 / -60.69	2.20 / -0.52
25 Jan 2016	72	-79.08 / -58.44	-81.28 / -57.92	2.20 / -0.52
25 Jan 2016	64	-37.33 / -55.34	-39.56 / -54.82	2.23 / -0.52
09 Mar 2016	88	-175.34 / -75.23	-175.33 / -75.10	-0.01 / -0.13
09 Mar 2016	80	-135.15 / -73.13	-135.15 / -73.00	0.00 / -0.13
09 Mar 2016	72	-101.59 / -70.14	-101.55 / -70.01	-0.04 / -0.13
09 Mar 2016	64	-71.08 / -66.81	-71.02 / -66.68	-0.06 / -0.13

0.03 Kd^{-1} (-0.15 Kd^{-1}) at the altitude of the maximum ΔH_{net} for sza = 88° (sza = 72°) on 25 January 2016. The corresponding change at the minimum ΔH_{net} results in 0.03 Kd^{-1} (-0.05 Kd^{-1}). On 09 March 2016 the maximum ΔH_{net} changes by 0.14 Kd^{-1} (-0.22 Kd^{-1}) for sza = 88° (sza = 72°), whereas the minimum differs by 0.06 Kd^{-1} (0.10 Kd^{-1}) for sza = 88° (sza = 72°). At the BOA all changes are in the order of 10^{-4} Kd^{-1}. Thus, the transition from the ocean surface to a bright snow surface results in small changes in the heating rate profiles, within the ice cloud and outside.

When multiplying the IWC by 5 (Fig. A3), $\Delta H_{\text{net}}(z)$ changes significantly in shape. On 25 January the maximum is 6.88 Kd^{-1} for sza = 72° and the minimum ΔH_{net} is -7.39 Kd^{-1} for sza = 88° . The corresponding maximum and minimum values on 09 March are 7.78 Kd^{-1} and -14.58 Kd^{-1}. The change in shape or vertical dependency is due to the high optical thicknesses of the clouds and manifests itself mainly in two features: First, the scaling of $\Delta H_{\text{net}}(z)$ with z is stronger at lower

Atmospheric
Chemistry
and Physics
Discussions
Open Access
EGU

altitudes than up higher, due to the higher absolute concentration of ice water in the thicker air at lower altitude. Second, the influence of the SW contribution is more limited to the uppermost cloud layers. This leads to a reduced warming impact of the

455   SW regime on the overall heating rate profile, especially in the 09 March case, where the majority of the IWC distribution is more centred in the cloud profile. Nonetheless, ΔH_{net} still remains negligible above and below the clouds.

6   Discussion and outlook

Our radiative transfer simulations for selected profiles of the IWC measured during the POLSTRACC campaign indicate that an ice cloud of extended geometrical thickness and a specific vertically asymmetric fine structure of the IWC changes the

460   radiation budget at the TOA when compared to the results of a vertically constant IWC profile of equal optical thickness. Effects are significant and for our cases in the order of a few Wm^{-2}. Fine structures in geometrically thin ice clouds having a more symmetric IWC profile do not lead to a noticeable modification of the TOA radiation budget when compared to the case of a vertically constant IWC. This is consistent with the results by Feofilov et al. (2015), who performed a statistical analysis of cirrus IWC profiles and their radiative effects from active and passive space-borne remote sensing products. Similar

465   to our above result, they conclude that the LW effect of a certain profile (at the TOA) is modulated by an "effective radiative layer" with respect to a constant IWC profile. The study by Feofilov et al. (2015) is dominated by low and midlatitude cirrus properties with higher IWP and optical thickness. In contrast, our analyses are focused on thinner Arctic cirrus clouds which exist in darkness or at high solar zenith angles such that their net radiative forcing may be of alternating sign.

A significant impact on net irradiances at the top and the bottom of the atmosphere is found to originate from the albedo of

470   typical Arctic surface types, such as the open ocean or snow covered regions, implying also effects on the radiative forcing. Effects depend on the solar zenith angle, except for the surface radiation budget over fresh fallen snow with a high albedo (e.g. $\alpha = 0.85$). Age and pollution of snow seem important factors in this context. For example, the transition from negative to positive values of the TOA radiation budget, equivalent to a change from a loss to a gain of radiative energy, occurs at a greater solar zenith angle over the ocean than for example over aged snow ($\alpha_{\mathrm{snow}} = 0.60$). Furthermore, over aged snow the

475   transition is shifted towards a higher solar zenith angle when compared to results for a cloud free atmosphere. This means that the presence of the cirrus leads to an enhanced gain of radiative energy in the Arctic atmosphere in most cases, except from the open ocean case on summer days around local noon. Therefore in scenarios with an overall negative trend of surface albedos in the Arctic, the positive radiative forcing effect of cirrus is expected to decrease. This is relevant in view of the Arctic amplification (e.g. Wendisch et al., 2017; Perovich and Polashenski, 2012; Thackeray and Hall, 2019). Notwithstanding, the

480   (direct) impact on surface net irradiances and therefore on surface temperature is much less pronounced.

Instantaneous heating rate profiles of the atmosphere are affected by fine structures of the IWC mainly within the cloud layer and remain negligible below and above the cloud. The effect of different surface albedo values on instantaneous heating rate profiles is only very weak. Depending on the profile of IWC or optical thickness, the heating rate profile can contribute to a strengthening or weakening of a given structure in the temperature profile, especially concerning the cold point of the

485   tropopause, as well as the strength of the above inversion layer. However, a heating rate profile first of all will trigger cloud

Atmospheric
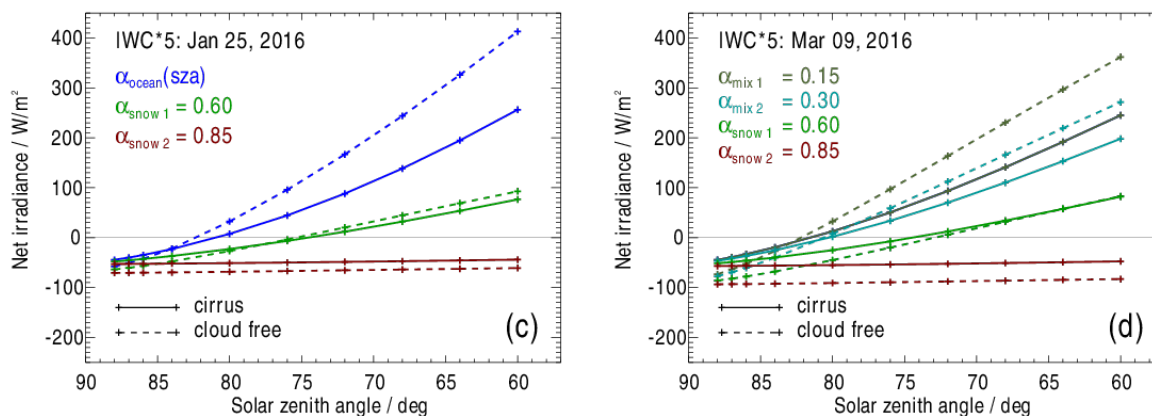Chemistry
and Physics
Discussions

Figure A1. Same as in Figs. 9a, b, but for ice clouds with higher optical thicknesses as a result of multiplying the entire profile IWC(z) with a factor of 5.

internal processes through evaporation or latent heat release, which drive vertical motion, modify the temperature gradient and change the microphysical properties of the ice particles.

Concerning a probable underestimation of IWC in the measurements, we derived that a potentially higher true IWC profile would lead, as can be expected, to a more warming impact of the cirrus on the TOA radiation budget and dampen the effect of

490 different surface albedo values. At the same time, the heating rate profiles would be more dominated by the LW contribution due to the strongly enhanced optical thickness. Still we conclude that our original calculations are of value because there exist (and have been observed) many thinner cirrus clouds in the Arctic to which our results would apply accordingly, beyond the two cases that we analysed.

Some aspects of Arctic ice clouds have not been treated in this work, notably effects of different ice crystal habits and the

495 modification of size and number density by specific cloud formation regimes. Recent and current observational activities will provide additional data on cloud microphysical properties to better represent real Arctic cirrus in similar studies, aiming for a closure of the physics of particle-scale processes with the radiation field. In this respect, the in situ measurements of the recent CIRRUS-HL mission are very promising. Further useful contributions are expected to come from ongoing and planned campaign activities.

500 **Appendix A: Appendix**

This appendix includes figures and a table similar to the respective instances in the main text. In this case, however, the radiative transfer calculations were carried out with IWC profiles that are scaled by a factor 5 compared to the profiles used in the main text, in order to account for the likely underestimation of IWC in the measurements.
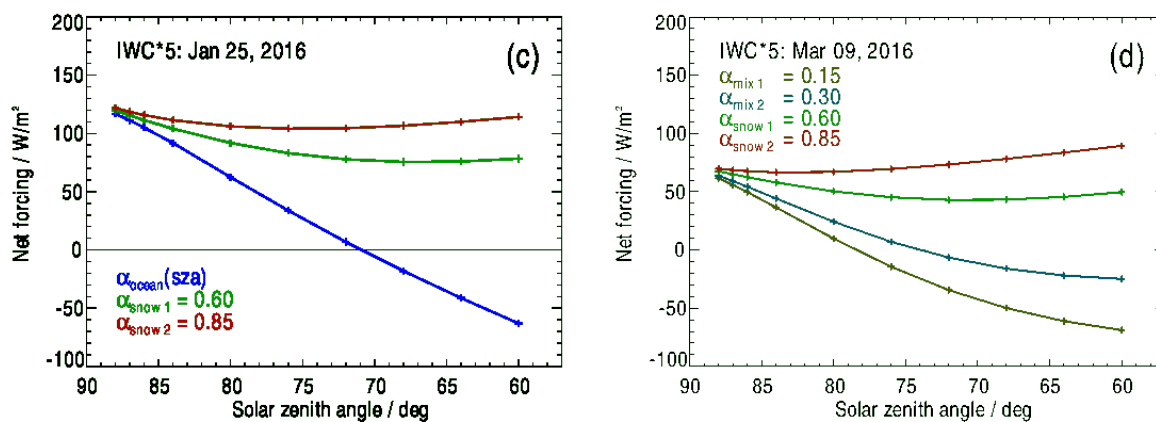
Atmospheric
Chemistry
and Physics
Discussions

Figure A2. Same as in Figs. 10a, b, but for ice clouds with higher optical thicknesses as a result of multiplying the entire profile IWC(z) with a factor of 5.
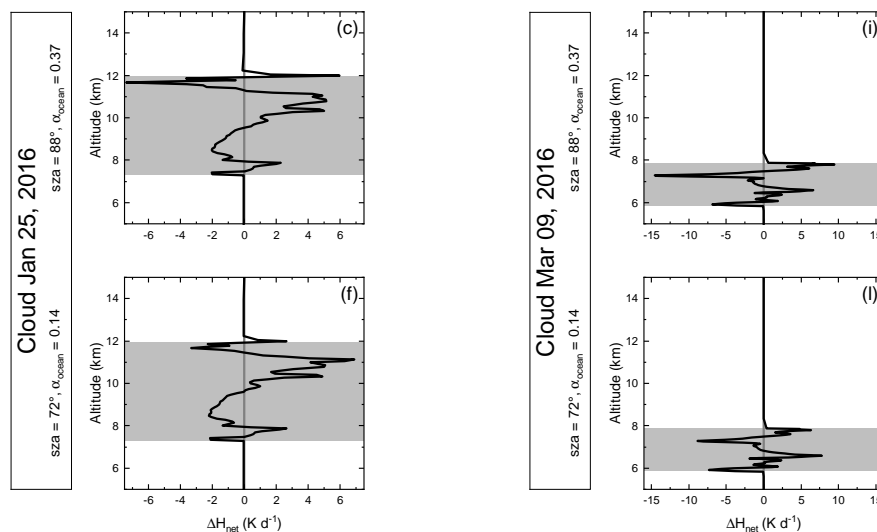

Figure A3. Same as in Fig. 12c, f, i, l, but for ice clouds with higher optical thicknesses as a result of multiplying the entire profile IWC(z) with a factor of 5.

Data availability. In situ observational data are available at the HALO database: https://https://halo-db.pa.op.dlr.de/. ECMWF model data are available at https://www.ecmwf.int. Results from the radiative transfer calculations are available from the contact author upon request.

Table A1. Same as in Tab. 2, but for ice clouds with higher optical thicknesses as a result of multiplying the entire profile IWC(z) with a factor of 5.

Date	sza	$F_{\rm net,TOA}$ / $F_{\rm net,BOA}$ for IWC(z)$_{\rm meas}$	$F_{\rm net,TOA}$ / $F_{\rm net,BOA}$ for IWC(z)$_{\rm const}$	$\Delta F_{\rm net,TOA}$ / $\Delta F_{\rm net,BOA}$ (measured - constant)
	(°)	(Wm^{-2})	(Wm^{-2})	(Wm^{-2})
$\alpha_{\rm ocean}$ (sza)				
25 Jan 2016	88	-93.41 / 8.72	-97.21 / 8.75	3.80 / -0.03
25 Jan 2016	80	-6.06 / 60.71	-10.22 / 60.78	4.16 / -0.07
25 Jan 2016	72	104.95 / 141.32	100.58 / 141.27	4.37 / 0.05
25 Jan 2016	64	240.98 / 247.94	236.36 / 247.72	4.62 / 0.22
09 Mar 2016	88	-131.51 / 9.65	-130.56 / 9.47	-0.95 / 0.18
09 Mar 2016	80	-40.16 / 64.94	-40.45 / 64.91	-0.29 / 0.03
09 Mar 2016	72	73.27 / 152.05	73.35 / 152.15	-0.08 / -0.10
09 Mar 2016	64	212.03 / 268.22	211.76 / 267.96	0.27 / 0.26
$\alpha_{\rm snow}$ = 0.85				
25 Jan 2016	88	-101.05 / 0.37	-104.87 / 0.37	3.82 / 0.00
25 Jan 2016	80	-59.31 / 2.13	-63.54 / 2.13	4.23 / 0.00
25 Jan 2016	72	-19.12 / 4.56	-23.45 / 4.57	4.33 / -0.01
25 Jan 2016	64	23.46 / 7.51	18.98 / 7.52	4.48 / -0.01
09 Mar 2016	88	-139.32 / 0.41	-139.05 / 0.41	-0.27 / 0.00
09 Mar 2016	80	-97.72 / 2.25	-97.25 / 2.25	-0.47 / 0.00
09 Mar 2016	72	-61.64 / 4.85	-61.52 / 4.86	0.12 / -0.01
09 Mar 2016	64	-25.55 / 8.01	-25.69 / 8.02	-0.14 / -0.01

References

Afchine, A., Rolf, C., Costa, A., Spelten, N., Riese, M., Buchholz, B., Ebert, V., Heller, R., Kaufmann, S., Minikin, A., Voigt, C., Zöger, M., Smith, J., Lawson, P., Lykov, A., Khaykin, S., and Krämer, M.: Ice particle sampling from aircraft – influence of the probing position on the ice water content, Atmos. Meas. Tech., 11, 4015–4031, https://doi.org/10.5194/amt-11-4015-2018, 2018.

Baum, B. A., Yang, P., Heymsfield, A. J., Platnick, S., King, M. D., Hu, Y.-X., and Bedka, S. T.: Bulk Scattering Properties for the Remote Sensing of Ice Clouds. Part II: Narrowband Models, J. Appl. Meteorol., 44, 1896–1911, https://doi.org/10.1175/jam2309.1, 2005.

Baum, B. A., Yang, P., Nasiri, S., Heidinger, A. K., Heymsfield, A., and Li, J.: Bulk Scattering Properties for the Remote Sensing of Ice Clouds. Part III: High-Resolution Spectral Models from 100 to 3250 cm-1, J. Appl. Meteorol., 46, 423–434, https://doi.org/10.1175/jam2473.1, 2007.

Borrmann, S., Solomon, S., Dye, J. E., and Luo, B.: The potential of cirrus clouds for heterogeneous chlorine activation, Geophys. Res. Lett., 23, 2133–2136, https://doi.org/10.1029/96gl01957, 1996.

Braun, M., Grooß, J.-U., Woiwode, W., Johansson, S., Höpfner, M., Friedl-Vallon, F., Oelhaf, H., Preusse, P., Ungermann, J., Sinnhuber, B.-M., Ziereis, H., and Braesicke, P.: Nitrification of the lowermost stratosphere during the exceptionally cold Arctic winter 2015–2016, Atmos. Chem. Phys., 19, 13 681–13 699, https://doi.org/10.5194/acp-19-13681-2019, 2019.

Bucholtz, A., Hlavka, D. L., McGill, M. J., Schmidt, K. S., Pilewskie, P., Davis, S. M., Reid, E. A., and Walker, A. L.: Directly measured heating rates of a tropical subvisible cirrus cloud, J. Geophys. Res., 115, https://doi.org/10.1029/2009jd013128, 2010.

Ewald, F., Groß, S., Wirth, M., Delanoë, J., Fox, S., and Mayer, B.: Why we need radar, lidar, and solar radiance observations to constrain ice cloud microphysics, Atmos Meas Tech, 14, 5029–5047, https://doi.org/10.5194/amt-14-5029-2021, 2021.

Feofilov, A. G., Stubenrauch, C. J., and Delanoë, J.: Ice water content vertical profiles of high-level clouds: classification and impact on radiative fluxes, Atmos. Chem. Phys., 15, 12 327–12 344, https://doi.org/10.5194/acp-15-12327-2015, 2015.

Fusina, F. and Spichtinger, P.: Cirrus clouds triggered by radiation, a multiscale phenomenon, Atmos. Chem. Phys., 10, 5179–5190, https://doi.org/10.5194/acp-10-5179-2010, 2010.

Fusina, F., Spichtinger, P., and Lohmann, U.: Impact of ice supersaturated regions and thin cirrus on radiation in the midlatitudes, J. Geophys. Res., 112, https://doi.org/10.1029/2007jd008449, 2007.

Gardner, A. S. and Sharp, M. J.: A review of snow and ice albedo and the development of a new physically based broadband albedo parameterization, J. Geophys. Res., 115, https://doi.org/10.1029/2009jf001444, 2010.

Gettelman, A., Hoor, P., Pan, L. L., Randel, W. J., Hegglin, M. I., and Birner, T.: The extratropical upper troposphere and lower stratosphere, Rev. Geophys., 49, https://doi.org/10.1029/2011rg000355, 2011.

Giez, A., Mallaun, C., Zöger, M., Dörnbrack, A., and Schumann, U.: Static Pressure from Aircraft Trailing-Cone Measurements and Numerical Weather-Prediction Analysis, J. Aircraft, 54, 1728–1737, https://doi.org/10.2514/1.c034084, 2017.

Hallar, A. G., Avallone, L. M., Herman, R. L., Anderson, B. E., and Heymsfield, A. J.: Measurements of ice water content in tropopause region Arctic cirrus during the SAGE III Ozone Loss and Validation Experiment (SOLVE), J. Geophys. Res., 109, https://doi.org/10.1029/2003jd004348, 2004.

Heller, R.: Einfluss von Gebirgswellen auf die Wasserdampfverteilung in der oberen Troposphäre und unteren Stratosphäre, Ph.D. thesis, Ludwig-Maximilians-Universität München, https://doi.org/10.5282/EDOC.23745, 2018.

Heymsfield, A. J., Krämer, M., Luebke, A., Brown, P., Cziczo, D. J., Franklin, C., Lawson, P., Lohmann, U., McFarquhar, G., Ulanowski, Z., and Tricht, K. V.: Cirrus Clouds, Meteor. Monogr., 58, 21–226, https://doi.org/10.1175/amsmonographs-d-16-0010.1, 2017.

Hoinka, K. P.: Die Tropopause: Entdeckung, Definition, Bestimmung, Meteorol. Z., 6, 281–303, https://doi.org/10.1127/metz/6/1997/281, 1997.

Hong, Y. and Liu, G.: The Characteristics of Ice Cloud Properties Derived from Cloud Sat and CALIPSO Measurements, J. Clim., 28, 3880–3901, https://doi.org/10.1175/jcli-d-14-00666.1, 2015.

Hoose, C. and Möhler, O.: Heterogeneous ice nucleation on atmospheric aerosols: a review of results from laboratory experiments, Atmos. Chem. Phys., 12, 9817–9854, https://doi.org/10.5194/acp-12-9817-2012, 2012.

Johansson, S., Santee, M. L., Grooß, J.-U., Höpfner, M., Braun, M., Friedl-Vallon, F., Khosrawi, F., Kirner, O., Kretschmer, E., Oelhaf, H., Orphal, J., Sinnhuber, B.-M., Tritscher, I., Ungermann, J., Walker, K. A., and Woiwode, W.: Unusual chlorine partitioning in the 2015/16 Arctic winter lowermost stratosphere: observations and simulations, Atmos. Chem. Phys., 19, 8311–8338, https://doi.org/10.5194/acp-19-8311-2019, 2019.

Joos, H., Spichtinger, P., Reutter, P., and Fusina, F.: Influence of heterogeneous freezing on the microphysical and radiative properties of orographic cirrus clouds, Atmos. Chem. Phys., 14, 6835–6852, https://doi.org/10.5194/acp-14-6835-2014, 2014.

Keber, T., Bönisch, H., Hartick, C., Hauck, M., Lefrancois, F., Obersteiner, F., Ringsdorf, A., Schohl, N., Schuck, T., Hossaini, R., Graf, P., Jöckel, P., and Engel, A.: Bromine from short-lived source gases in the extratropical northern hemispheric upper troposphere and lower stratosphere (UTLS), Atmos. Chem. Phys., 20, 4105–4132, https://doi.org/10.5194/acp-20-4105-2020, 2020.

Krisch, I., Ern, M., Hoffmann, L., Preusse, P., Strube, C., Ungermann, J., Woiwode, W., and Riese, M.: Superposition of gravity waves with different propagation characteristics observed by airborne and space-borne infrared sounders, Atmos. Chem. Phys., 20, 11 469–11 490, https://doi.org/10.5194/acp-20-11469-2020, 2020.

Krisna, T. C., Wendisch, M., Ehrlich, A., Jäkel, E., Werner, F., Weigel, R., Borrmann, S., Mahnke, C., Pöschl, U., Andreae, M. O., Voigt, C., and Machado, L. A. T.: Comparing airborne and satellite retrievals of cloud optical thickness and particle effective radius using a spectral radiance ratio technique: two case studies for cirrus and deep convective clouds, Atmos. Chem. Phys., 18, 4439–4462, https://doi.org/10.5194/acp-18-4439-2018, 2018.

Krämer, M., Rolf, C., Luebke, A., Afchine, A., Spelten, N., Costa, A., Meyer, J., Zöger, M., Smith, J., Herman, R. L., Buchholz, B., Ebert, V., Baumgardner, D., Borrmann, S., Klingebiel, M., and Avallone, L.: A microphysics guide to cirrus clouds – Part 1: Cirrus types, Atmos. Chem. Phys., 16, 3463–3483, https://doi.org/10.5194/acp-16-3463-2016, 2016.

Krämer, M., Rolf, C., Spelten, N., Afchine, A., Fahey, D., Jensen, E., Khaykin, S., Kuhn, T., Lawson, P., Lykov, A., Pan, L. L., Riese, M., Rollins, A., Stroh, F., Thornberry, T., Wolf, V., Woods, S., Spichtinger, P., Quaas, J., and Sourdeval, O.: A microphysics guide to cirrus – Part 2: Climatologies of clouds and humidity from observations, Atmos. Chem. Phys., 20, 12 569–12 608, https://doi.org/10.5194/acp-20-12569-2020, 2020.

Kärcher, B.: Formation and radiative forcing of contrail cirrus, Nat. Commun., 9, https://doi.org/10.1038/s41467-018-04068-0, 2018.

Kärcher, B. and Jensen, E. J.: Microscale characteristics of homogeneous freezing events in cirrus clouds, Geophys. Res. Lett., https://doi.org/10.1002/2016gl072486, 2017.

Kärcher, B. and Voigt, C.: Formation of nitric acid/water ice particles in cirrus clouds, Geophys. Res. Lett., 33, https://doi.org/10.1029/2006gl025927, 2006.

Kärcher, B., Abbatt, J. P. D., Cox, R. A., Popp, P. J., and Voigt, C.: Trapping of trace gases by growing ice surfaces including surface-saturated adsorption, J. Geophys. Res., 114, https://doi.org/10.1029/2009jd011857, 2009.

Liou, K. N., Gu, Y., Yue, Q., and McFarguhar, G.: On the correlation between ice water content and ice crystal size and its application to radiative transfer and general circulation models, Geophys. Res. Lett., 35, https://doi.org/10.1029/2008gl033918, 2008.

Luebke, A. E., Avallone, L. M., Schiller, C., Meyer, J., Rolf, C., and Krämer, M.: Ice water content of Arctic, midlatitude, and tropical cirrus – Part 2: Extension of the database and new statistical analysis, Atmos. Chem. Phys., 13, 6447–6459, https://doi.org/10.5194/acp-13-6447-2013, 2013.

590   Marsing, A., Jurkat-Witschas, T., Grooß, J.-U., Kaufmann, S., Heller, R., Engel, A., Hoor, P., Krause, J., and Voigt, C.: Chlorine partitioning in the lowermost Arctic vortex during the cold winter 2015/2016, Atmos. Chem. Phys., 19, 10 757–10 772, https://doi.org/10.5194/acp-19-10757-2019, 2019.

Mayer, B. and Kylling, A.: Technical note: The libRadtran software package for radiative transfer calculations - description and examples of use, Atmos. Chem. Phys., 5, 1855–1877, https://doi.org/10.5194/acp-5-1855-2005, 2005.

595   Meyer, J., Rolf, C., Schiller, C., Rohs, S., Spelten, N., Afchine, A., Zöger, M., Sitnikov, N., Thornberry, T. D., Rollins, A. W., Bozóki, Z., Tátrai, D., Ebert, V., Kühnreich, B., Mackrodt, P., Möhler, O., Saathoff, H., Rosenlof, K. H., and Krämer, M.: Two decades of water vapor measurements with the FISH fluorescence hygrometer: a review, Atmos. Chem. Phys., 15, 8521–8538, https://doi.org/10.5194/acp-15-8521-2015, 2015.

Oelhaf, H., Sinnhuber, B.-M., Woiwode, W., Bönisch, H., Bozem, H., Engel, A., Fix, A., Friedl-Vallon, F., Grooß, J.-U., Hoor, P., Johansson,

600   S., Jurkat-Witschas, T., Kaufmann, S., Krämer, M., Krause, J., Kretschmer, E., Lörks, D., Marsing, A., Orphal, J., Pfeilsticker, K., Pitts, M., Poole, L., Preusse, P., Rapp, M., Riese, M., Rolf, C., Ungermann, J., Voigt, C., Volk, C. M., Wirth, M., Zahn, A., and Ziereis, H.: POLSTRACC: Airborne Experiment for Studying the Polar Stratosphere in a Changing Climate with the High Altitude and Long Range Research Aircraft (HALO), Bull. Amer. Meteor. Soc., 100, 2634–2664, https://doi.org/10.1175/bams-d-18-0181.1, 2019.

Payne, R. E.: Albedo of the Sea Surface, J. Atmos. Sci., 29, 959–970, https://doi.org/10.1175/1520-0469(1972)029<0959:aotss>2.0.co;2,

605   1972.

Perovich, D. K. and Polashenski, C.: Albedo evolution of seasonal Arctic sea ice, Geophys. Res. Lett., 39, n/a–n/a, https://doi.org/10.1029/2012gl051432, 2012.

Pitts, M. C., Poole, L. R., and Gonzalez, R.: Polar stratospheric cloud climatology based on CALIPSO spaceborne lidar measurements from 2006 to 2017, Atmos. Chem. Phys., 18, 10 881–10 913, https://doi.org/10.5194/acp-18-10881-2018, 2018.

610   Sassen, K., Wang, Z., and Liu, D.: Global distribution of cirrus clouds from CloudSat/Cloud-Aerosol Lidar and Infrared Pathfinder Satellite Observations (CALIPSO) measurements, J. Geophys. Res., 113, https://doi.org/10.1029/2008jd009972, 2008.

Schiller, C., Afchine, A., Eicke, N., Feigl, C., Fischer, H., Giez, A., Konopka, P., Schlager, H., Tuitjer, F., Wienhold, F. G., and Zöger, M.: Ice particle formation and sedimentation in the tropopause region: A case study based on in situ measurements of total water during POLSTAR 1997, Geophys. Res. Lett., 26, 2219–2222, https://doi.org/10.1029/1999gl900337, 1999.

615   Schiller, C., Bauer, R., Cairo, F., Deshler, T., Dörnbrack, A., Elkins, J., Engel, A., Flentje, H., Larsen, N., Levin, I., Müller, M., Oltmans, S., Ovarlez, H., Ovarlez, J., Schreiner, J., Stroh, F., Voigt, C., and Vömel, H.: Dehydration in the Arctic stratosphere during the SOLVE/THESEO-2000 campaigns, J. Geophys. Res., 107, https://doi.org/10.1029/2001jd000463, 2002.

Schiller, C., Krämer, M., Afchine, A., Spelten, N., and Sitnikov, N.: Ice water content of Arctic, midlatitude, and tropical cirrus, J. Geophys. Res. Atmos., 113, https://doi.org/10.1029/2008JD010342, 2008.

620   Shupe, M. D., Rex, M., Blomquist, B., Persson, P. O. G., Schmale, J., Uttal, T., Althausen, D., Angot, H., Archer, S., Bariteau, L., Beck, I., Bilberry, J., Bucci, S., Buck, C., Boyer, M., Brasseur, Z., Brooks, I. M., Calmer, R., Cassano, J., Castro, V., Chu, D., Costa, D., Cox, C. J., Creamean, J., Crewell, S., Dahlke, S., Damm, E., de Boer, G., Deckelmann, H., Dethloff, K., Dütsch, M., Ebell, K., Ehrlich, A., Ellis, J., Engelmann, R., Fong, A. A., Frey, M. M., Gallagher, M. R., Ganzeveld, L., Gradinger, R., Graeser, J., Greenamyer, V., Griesche, H., Griffiths, S., Hamilton, J., Heinemann, G., Helmig, D., Herber, A., Heuzé, C., Hofer, J., Houchens, T., Howard, D., Inoue, J., Jacobi, H.-

625   W., Jaiser, R., Jokinen, T., Jourdan, O., Jozef, G., King, W., Kirchgaessner, A., Klingebiel, M., Krassovski, M., Krumpen, T., Lampert, A.,
       Landing, W., Laurila, T., Lawrence, D., Lonardi, M., Loose, B., Lüpkes, C., Maahn, M., Macke, A., Maslowski, W., Marsay, C., Maturilli,
       M., Mech, M., Morris, S., Moser, M., Nicolaus, M., Ortega, P., Osborn, J., Pätzold, F., Perovich, D. K., Petäjä, T., Pilz, C., Pirazzini, R.,
       Posman, K., Powers, H., Pratt, K. A., Preußer, A., Quéléver, L., Radenz, M., Rabe, B., Rinke, A., Sachs, T., Schulz, A., Siebert, H., Silva,
       T., Solomon, A., Sommerfeld, A., Spreen, G., Stephens, M., Stohl, A., Svensson, G., Uin, J., Viegas, J., Voigt, C., von der Gathen, P.,
630   Wehner, B., Welker, J. M., Wendisch, M., Werner, M., Xie, Z., and Yue, F.: Overview of the MOSAiC expedition: Atmosphere, Elem. Sci.
       Anth., 10, https://doi.org/10.1525/elementa.2021.00060, 2022.

       Solomon, S., Borrmann, S., Garcia, R. R., Portmann, R., Thomason, L., Poole, L. R., Winker, D., and McCormick, M. P.: Heterogeneous
       chlorine chemistry in the tropopause region, J. Geophys. Res. Atmos., 102, 21 411–21 429, https://doi.org/10.1029/97jd01525, 1997.

       Strandgren, J., Bugliaro, L., Sehnke, F., and Schröder, L.: Cirrus cloud retrieval with MSG/SEVIRI using artificial neural networks, Atmos.
635   Meas. Tech., 10, 3547–3573, https://doi.org/10.5194/amt-10-3547-2017, 2017.

       Thackeray, C. W. and Hall, A.: An emergent constraint on future Arctic sea-ice albedo feedback, Nat. Clim. Change, 9, 972–978,
       https://doi.org/10.1038/s41558-019-0619-1, 2019.

       Thornberry, T. D., Rollins, A. W., Avery, M. A., Woods, S., Lawson, R. P., Bui, T. V., and Gao, R.-S.: Ice water content-extinction relationships
       and effective diameter for TTL cirrus derived from in situ measurements during ATTREX 2014, J. Geophys. Res. Atmos., 122, 4494–4507,
640   https://doi.org/10.1002/2016jd025948, 2017.

       Voigt, C., Schlager, H., Ziereis, H., Kärcher, B., Luo, B. P., Schiller, C., Krämer, M., Popp, P. J., Irie, H., and Kondo, Y.: Nitric acid in cirrus
       clouds, Geophys. Res. Lett., 33, https://doi.org/10.1029/2005gl025159, 2006.

       Voigt, C., Kärcher, B., Schlager, H., Schiller, C., Krämer, M., de Reus, M., Vössing, H., Borrmann, S., and Mitev, V.: In-situ observations
       and modeling of small nitric acid-containing ice crystals, Atmos. Chem. Phys., 7, 3373–3383, https://doi.org/10.5194/acp-7-3373-2007,
645   2007.

       Voigt, C., Jessberger, P., Jurkat, T., Kaufmann, S., Baumann, R., Schlager, H., Bobrowski, N., Giuffrida, G., and Salerno, G.: Evolution of
       CO_2, SO_2, HCl, and HNO_3 in the volcanic plumes from Etna, Geophys. Res. Lett., 41, 2196–2203, https://doi.org/10.1002/2013gl058974,
       2014.

       Voigt, C., Schumann, U., Minikin, A., Abdelmonem, A., Afchine, A., Borrmann, S., Boettcher, M., Buchholz, B., Bugliaro, L., Costa, A.,
650   Curtius, J., Dollner, M., Dörnbrack, A., Dreiling, V., Ebert, V., Ehrlich, A., Fix, A., Forster, L., Frank, F., Fütterer, D., Giez, A., Graf,
       K., Grooß, J.-U., Groß, S., Heimerl, K., Heinold, B., Hüneke, T., Järvinen, E., Jurkat, T., Kaufmann, S., Kenntner, M., Klingebiel, M.,
       Klimach, T., Kohl, R., Krämer, M., Krisna, T. C., Luebke, A., Mayer, B., Mertes, S., Molleker, S., Petzold, A., Pfeilsticker, K., Port, M.,
       Rapp, M., Reutter, P., Rolf, C., Rose, D., Sauer, D., Schäfler, A., Schlage, R., Schnaiter, M., Schneider, J., Spelten, N., Spichtinger, P.,
       Stock, P., Walser, A., Weigel, R., Weinzierl, B., Wendisch, M., Werner, F., Wernli, H., Wirth, M., Zahn, A., Ziereis, H., and Zöger, M.:
655   ML-CIRRUS: The Airborne Experiment on Natural Cirrus and Contrail Cirrus with the High-Altitude Long-Range Research Aircraft
       HALO, Bull. Amer. Meteor. Soc., 98, 271–288, https://doi.org/10.1175/bams-d-15-00213.1, 2017.

       Voigt, C., Dörnbrack, A., Wirth, M., Groß, S. M., Pitts, M. C., Poole, L. R., Baumann, R., Ehard, B., Sinnhuber, B.-M., Woiwode, W., and
       Oelhaf, H.: Widespread polar stratospheric ice clouds in the 2015–2016 Arctic winter – implications for ice nucleation, Atmos. Chem.
       Phys., 18, 15 623–15 641, https://doi.org/10.5194/acp-18-15623-2018, 2018.

660   von Hobe, M., Grooß, J.-U., Günther, G., Konopka, P., Gensch, I., Krämer, M., Spelten, N., Afchine, A., Schiller, C., Ulanovsky, A.,
       Sitnikov, N., Shur, G., Yushkov, V., Ravegnani, F., Cairo, F., Roiger, A., Voigt, C., Schlager, H., Weigel, R., Frey, W., Borrmann, S.,

Müller, R., and Stroh, F.: Evidence for heterogeneous chlorine activation in the tropical UTLS, Atmos. Chem. Phys., 11, 241–256, https://doi.org/10.5194/acp-11-241-2011, 2011.

Wendisch, M., Brückner, M., Burrows, J., Crewell, S., Dethloff, K., Ebell, K., Lüpkes, C., Macke, A., Notholt, J., Quaas, J., Rinke, A., and
665   Tegen, I.: Understanding Causes and Effects of Rapid Warming in the Arctic, Eos, https://doi.org/10.1029/2017eo064803, 2017.

Wolf, V., Kuhn, T., Milz, M., Voelger, P., Krämer, M., and Rolf, C.: Arctic ice clouds over northern Sweden: microphysical properties studied with the Balloon-borne Ice Cloud particle Imager B-ICI, Atmos. Chem. Phys., 18, 17 371–17 386, https://doi.org/10.5194/acp-18-17371-2018, 2018.

Zahn, A., Weppner, J., Widmann, H., Schlote-Holubek, K., Burger, B., Kühner, T., and Franke, H.: A fast and precise chemiluminescence
670   ozone detector for eddy flux and airborne application, Atmos. Meas. Tech., 5, 363–375, https://doi.org/10.5194/amt-5-363-2012, 2012.

Ziereis, H., Hoor, P., Grooß, J.-U., Zahn, A., Stratmann, G., Stock, P., Lichtenstern, M., Krause, J., Bense, V., Afchine, A., Rolf, C., Woiwode, W., Braun, M., Ungermann, J., Marsing, A., Voigt, C., Engel, A., Sinnhuber, B.-M., and Oelhaf, H.: Redistribution of total reactive nitrogen in the lowermost Arctic stratosphere during the cold winter 2015/2016, Atmos. Chem. Phys., 22, 3631–3654, https://doi.org/10.5194/acp-22-3631-2022, 2022.